



# ZIF-derived non-bonding Co/Zn coordinated hollow carbon nitride for enhanced removal of antibiotic contaminants by peroxyomonosulfate activation: Performance and mechanism

Xi Li <sup>a</sup>, Shiwen Wang <sup>a</sup>, Pei Chen <sup>a</sup>, Baokang Xu <sup>a</sup>, Xiao Zhang <sup>a,b</sup>, Yanhua Xu <sup>a</sup>, Ru Zhou <sup>c</sup>, Yang Yu <sup>d</sup>, Huaili Zheng <sup>e</sup>, Peng Yu <sup>a,\*</sup>, Yongjun Sun <sup>f,\*</sup>

<sup>a</sup> School of Environmental Science and Engineering, Nanjing Tech University, Nanjing 211816, China

<sup>b</sup> Key Laboratory of Industrial Pollution Control and Resource Reuse of Jiangsu Province, College of Environmental Engineering, Xuzhou University of Technology, Xuzhou 221000, China

<sup>c</sup> College of Safety Science and Engineering, Nanjing Tech University, Nanjing 211816, China

<sup>d</sup> Graduate School at Shenzhen, Tsinghua University, Shenzhen 518055, China

<sup>e</sup> Key Laboratory of the Three Gorges Reservoir Region's Eco-Environment, State Ministry of Education, Chongqing University, Chongqing 400045, China

<sup>f</sup> College of Urban Construction, Nanjing Tech University, Nanjing 211816, China



## ARTICLE INFO

### Keywords:

Antibiotic contaminants  
Peroxyomonosulfate activation  
Metal-organic frameworks  
Bimetallic active sites  
Non-bonding interaction

## ABSTRACT

Co–Zn–N–C catalyst (MCZC) with neighboring Co and Zn pairs anchored on hollow carbon nitride was constructed by the direct etching of zeolitic imidazolate frameworks assembled with Co and Zn. Adequate characterizations and density functional theory (DFT) studies confirmed the successful construction of non-bonding Co and Zn pairs with enhanced electron transfer on Co sites by adjacent Zn sites. Based on the synergy of adjacent Co and Zn atom pairs, the MCZC/Perxymosulfate (PMS) system achieved 99.6% Tetracycline (TC) degradation in 24 min with a mineralization rate of 55.8% and PMS decomposition efficiency of 73.1%. DFT calculation based on the Fukui index identified the sites susceptible to attack by the active species. TC degradation pathways could be inferred, and reduced toxicity of intermediates was observed. This work provides new insights into the design of MOF-derived bimetallic catalysts and the importance of the interaction between adjacent metal active sites to catalytic performance.

## 1. Introduction

The widespread use of antibiotics in various fields such as animal husbandry, agriculture, medicine, and aquaculture has led to the emergence of antibiotic-resistant genes (ARGs) and antibiotic-resistant bacteria (ARBs) in nature, especially in the aquatic environment [1,2]. Given their deleterious effects on humans and the ecosystem, the World Health Organization has identified them as one of the top three public health hazards of the 21st century [3]. Therefore, an effective approach to antibiotic contaminant control is urgently needed to reduce environmental risks. Interestingly, heterogeneous advanced oxidation technologies (AOPs) based on  $\text{SO}_4^{\cdot-}$  have demonstrated excellent performance in removing antibiotics from water [4]. An increasing body of evidence suggests that  $\text{SO}_4^{\cdot-}$  possesses a higher oxidation potential (2.5–3.1 V), a more comprehensive pH adaptation range (2–9), a longer

half-life (30–40  $\mu\text{s}$ ) than  $\text{HO}^{\cdot}$ , and is generally produced by activation of peroxyomonosulfate (PMS) or peroxydisulfate (PS) [5,6]. It has been reported that transition metal loaded on multiple carriers including metal oxides [7], molecular sieve [8], carbon materials [9], and metallic glasses [10–13] could effectively activate PMS, among which the heterogeneous Co-based catalysts exhibit better performance in PMS activation for the higher standard reduction potential of Co (III)/Co (II) (1.92 V) to that of  $\text{HSO}_5^-/\text{SO}_4^{2-}$  (1.82 V) than other metals including Fe, Mn, Ce and V [14]. However, avoiding natural diffusion and agglomeration remains challenging while constructing Co-based catalysts with high dispersion and low Co leaching amount to avoid the potential environmental risks.

In recent years, graphite carbon nitride ( $\text{g-C}_3\text{N}_4$ ) has attracted much attention given its unique  $\pi$ -conjugated electronic structure, excellent chemical and thermal stability, and potential application prospects [15].

\* Corresponding authors.

E-mail addresses: [yspong@163.com](mailto:yspong@163.com) (P. Yu), [sunyongjun@njtech.edu.cn](mailto:sunyongjun@njtech.edu.cn) (Y. Sun).

In this respect,  $\text{g-C}_3\text{N}_4$  has demonstrated significant benefits in anchoring and dispersing metal atoms, as its lone electron pair at the nitrogen site is not only the key to the electronic structure of  $\text{g-C}_3\text{N}_4$  but also capable of stabilizing metal atoms with the formation of metal-N coordination bond [16,17]. However, conventional metal-doped  $\text{g-C}_3\text{N}_4$  synthesis often results in severe specific surface area ( $S_{\text{BET}}$ ) decay and porosity reduction due to the thermal polymerization process, which directly leads to insufficient exposure of the active metal site and limits its further environmental application [18,19]. It has been reported that using unsaturated cyanuric acid or prefabricated molecular cooperative assembly as a precursor might modify the polycondensation and the chemical structure of  $\text{g-C}_3\text{N}_4$  with the formation of a significantly porous structure that could facilitate electron transfer and delocalization [20]. There is a rich literature suggesting that constructing a 3D structure can expand the  $S_{\text{BET}}$  and the exposure of active sites and provide more pathways for electron transfer [21,22].

Overwhelming evidence substantiates that metal-organic frameworks (MOFs), consisting of metal ligands and organic skeletons, exhibit great potential in many fields due to their ultrahigh surface area, tunable pore size, and well-defined and tailorabile structure [23–25]. In this respect, MOF's structural and component modulation advantages account for its great potential for constructing catalysts with high active component dispersion [26]. It has been reported that the transition metals encapsulated in the nitrogen-doped complexes can further enhance catalytic activity through a synergistic effect between the nitrogen-doped carbon and the transition metals while improving catalyst stability [27]. Moreover, the ordered organic coordination structure in MOF could facilitate the formation of nitrogen-doped metal-N-C (M-N-C) with uniform heteroatoms distribution, which could achieve long-range electron delocalization and is promising to couple adjacent non-bonding single metal atoms with planar and conjugated carbon structure [28,29]. In our previous work, an efficient method of anchoring exposed Co sites on porous carbon nitride by etching ZIF-67 was reported, and the synthesized catalyst yielded excellent PMS activation performance [30]. The identical prismatic dodecahedral structures of zeolitic imidazolate framework-67 (ZIF-67, Co) and zeolitic imidazolate framework-8 (ZIF-8, Zn) and the same organic ligand (dimethylimidazole) provide an ideal platform for the precise construction of MOF-derived Co-Zn-N-C materials [31], including MOF-derived non-bonded Co, Zn co-doped porous carbon nitride.

In the present study, we designed a derivative bimetallic co-doped porous carbon nitride catalyst to enhance PMS activation by coupling non-bonded Co and Zn sites while reducing the content of Co. Tetracycline (TC), a typical and widely used antibiotic with high toxicity, was chosen as a mimetic contaminant [32]. The morphological structure and chemical composition of the synthesized catalysts were characterized. The influences of the Co/Zn coordinated zeolitic imidazolate framework (Co/Zn-ZIF) addition, catalyst dose, PMS concentration, pH, and co-existing ions on TC degradation were systematically studied. Density functional theory (DFT) calculations were used to elucidate the compositional morphology of the catalysts and the auxiliary catalytic effect of Zn. The primary active species in the degradation process were identified to reveal the catalytic mechanism. The possible TC degradation pathways were further inferred and the toxicities of intermediates were accurately predicted.

## 2. Materials and method

### 2.1. Chemicals and reagents

All chemicals and reagents in this work were analytical-grade (AG) or high-performance liquid chromatography (HPLC) grade reagents without any purification. Cobalt nitrate hexahydrate ( $\text{Co}(\text{NO}_3)_2 \cdot 6 \text{H}_2\text{O}$ ), zinc nitrate hexahydrate ( $\text{Zn}(\text{NO}_3)_2 \cdot 6 \text{H}_2\text{O}$ ), potassium iodide (KI),  $\text{Na}_2\text{S}_2\text{O}_3$ , NaCl,  $\text{Na}_2\text{CO}_3$ ,  $\text{NaHCO}_3$ ,  $\text{Na}_2\text{SO}_4$ ,  $\text{NaH}_2\text{PO}_4$ , and NaOH were all purchased from Sinopharm Chemical Reagents Co., Ltd. (Nanjing,

China). Tetracycline (TC), peroxymonosulfate (PMS), dimethylimidazole ( $\text{C}_4\text{H}_6\text{N}_2$ ), melamine (MA), cyanuric acid (CA), methanol (MeOH), ethanol (EtOH), humic acid (HA), tert-butyl alcohol (TBA), L-histidine (L-his), *p*-benzoquinone (*p*-BQ), dimethyl sulfoxide (DMSO), 5,5-Dimethyl-1-pyrroline-N-oxide (DMPO) and 2,2,6,6-tetramethyl-4-piperidone (TEMP) were provided by Aladdin Chemical Co., Ltd (Shanghai, China). Deionized water used in all experiments was generated by a water purification instrument (GWB-UP, Persee, China). Tap water was supplied by Nanjing Chemical Industrial Park Water Industry Co., Ltd. (Nanjing, China).

### 2.2. Synthesis of catalysts

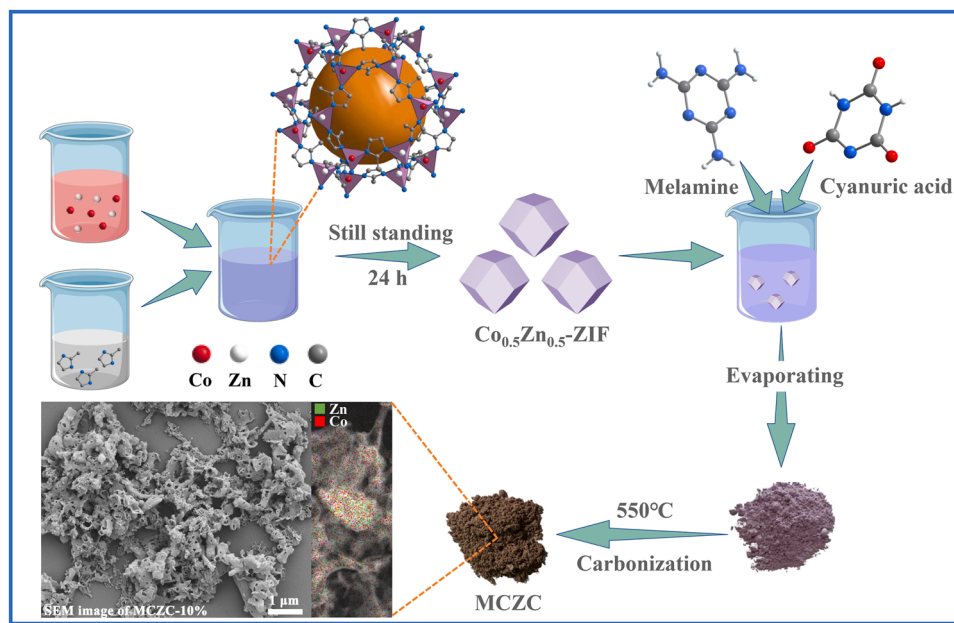
The Zn/Co-ZIF was synthesized by a modified method for ZIF-67 preparation [33]. A mixture of methanolic solutions of zinc nitrate (5 mM, 50 mL) and cobalt nitrate (5 mM, 50 mL) ultrasonicated for 10 min was added to a methanolic solution of dimethylimidazole (40 mM, 100 mL) and kept at room temperature for 24 h without stirring. The lavender precipitate at the bottom of the beaker was washed by centrifugation with methanol and deionized water several times and then dried under vacuum at 80 °C for 24 h to obtain the final ZIF material with Co and Zn as metallic arrays, named  $\text{Co}_{0.5}\text{Zn}_{0.5}\text{-ZIF}$ . ZIF-67 and ZIF-8 were synthesized using the same method by adding only Cobalt nitrate (10 mM, 100 mL) or zinc nitrate (10 mM, 100 mL).

ZIF-derived non-bonding Co/Zn coordinated hollow carbon nitride was synthesized by the method reported in our previous work [30]. According to the recommended synthesis procedure (Scheme 1.), 1 g of MA was added to a well-dispersed  $\text{Co}_{0.5}\text{Zn}_{0.5}\text{-ZIF}$  aqueous solution (0.1 g, 40 mL) with continuous stirring for 1 h. Subsequently, the CA dispersion (1 g 40 mL) was added to the previously mixed solution and stirred for another 30 min before complete water evaporation at 85 °C. The lavender precursor was well ground and carbonized at 550 °C (5 °C/min) under a nitrogen atmosphere for 240 min to obtain the final catalyst, MCZC-10%. Catalysts with different  $\text{Co}_{0.5}\text{Zn}_{0.5}\text{-ZIF}$  additions (0.05, 0.15 and 0.2 g) were prepared by the same method and named as MCZC-5%, MCZC-15%, MCZC-20%.

Porous carbon nitride was synthesized using the same method with no addition of  $\text{Co}_{0.5}\text{Zn}_{0.5}\text{-ZIF}$  and named PCN. ZIF-67-derived Co-doped porous carbon nitride was synthesized by the same method with the addition of ZIF-67 and named ZCCN.

### 2.3. Characterization

Morphology investigation was recorded by scanning electron microscope (SEM, Supra 55, Carl Zeiss, Germany). Transmission electron microscope (TEM) and high-resolution TEM (HRTEM) were performed on a JEM-200CX instrument (JEOL, Japan) with energy dispersive spectroscopy (EDS) applied to analyze the elemental composition and distribution. X-ray diffraction (XRD) analysis was carried out on a DMAX-2400 diffractometer (Rigaku, Japan) at 40 kV and 40 mA with Cu K $\alpha$  radiation ( $\lambda = 0.15406 \text{ \AA}$ ). The Raman spectra were recorded with a high-resolution Raman spectrophotometer LabRAM HR Evolution (HORIBA, Japan). The elemental composition and oxidation states were obtained by a Nexsa X-ray photoelectron spectroscopy (XPS, Thermo Fisher, USA) with all the binding energies calibrated with the peak of 284.8 eV on the C 1 s spectrum. Fourier transform infrared spectra (FTIR) were obtained by IRAffinity-1S FTIR spectrophotometer (Shimadzu, Japan). The zeta potentials of the synthesized catalysts were measured by a 90PlusPALS zeta analyzer (Brookhaven, USA).  $\text{N}_2$  adsorption-desorption analysis was performed on ASAP 2460 instrument (Micromeritics, USA). Electron paramagnetic resonance (EPR) signals of the generated free radicals were examined by an A300 spectrometer (Bruker, Germany) with DMPO and TEMP as the spin-trappers. Electrochemical tests, including linear sweep voltammetry (LSV), cyclic voltammetry (CV), and electrochemical impedance spectra (EIS), were carried out on an electrochemical workstation (CHI660E, CHI



**Scheme 1.** Synthesis of MCZC catalyst.

Instruments Inc., USA) with detailed information presented in Text S1 of supporting information.

#### 2.4. Experimental procedure and analysis

The experiment on PMS activation for TC degradation was performed in a 200 mL conical flask. Specifically, the catalyst was added to the TC solution (10 mg·L<sup>-1</sup>) and stirred for 30 min to reach adsorption equilibrium. Subsequently, PMS was added to the mixture with continuous stirring. Then, 1.5 mL of the solution was quickly drawn every 3 min and immediately filtered through a filter membrane (0.22 μm, polyethersulfone) before injection into a brown sample bottle pre-loaded with Na<sub>2</sub>S<sub>2</sub>O<sub>3</sub> solution (0.2 M, 50 μL) to quench the residual active species produced by PMS. The initial pH of the solution was adjusted using diluted NaOH solution (0.1 M) and HCl solution (0.1 M). The influence of Co<sub>0.5</sub>Zn<sub>0.5</sub>-ZIF addition, catalyst dosage, water chemistry (pH, inorganic ions [Cl<sup>-</sup>, SO<sub>4</sub><sup>2-</sup>, NO<sub>3</sub><sup>-</sup>, H<sub>2</sub>PO<sub>4</sub><sup>-</sup>, CO<sub>3</sub><sup>2-</sup>], and natural organic matter [HA]) and water matrix on the performance of MCZC/PMS system in TC degradation were systematically investigated. Details of the analysis methods and instruments, PMS consumption, the contributions of reactive species, and catalyst reuse performance tests are provided in Text S2 of supporting information.

#### 2.5. Theoretical computation

The DFT calculations were carried out using the Vienna Ab-initio Simulation Package (VASP) [34,35] with the frozen-core all-electron projector-augment-wave (PAW) method [36,37]. The Perdew-Burke-Ernzerhof (PBE) of generalized gradient approximation (GGA) was adopted to describe the exchange and correlation potential [38]. The cutoff energy for the plane-wave basis set was set to 450 eV. The Monkhorst-Pack k-point sampling was set to 3 × 3 × 1 for monolayer 2 × 2 graphene C<sub>3</sub>N<sub>4</sub> supercell [39]. A vacuum region of 20 Å was added above monolayer carbon nitride to minimize the interactions between neighboring systems. The geometry optimizations were performed until the forces on each ion were reduced below 0.01 eV/Å. The resulting structures were then used to calculate the electronic structures.

### 3. Results and discussion

#### 3.1. Characterization

The morphologies of the synthesized catalysts were investigated by SEM and TEM. The synthesized ZIF-67 showed a prismatic dodecahedral structure with an average size of 0.41 μm (Fig. 1a). After carbonization at 550 °C, although the relatively intact skeleton structure was maintained, polycondensation could be observed on the surface (Fig. 1b). Moreover, the synthesized ZCCN-10% catalyst exhibited abundant porous structures. In our previous study, we found that g-C<sub>3</sub>N<sub>4</sub> synthesized with MA and CA as precursors exhibited pore structure for the larger pore structure generated during the polycondensation at 400 °C collapsed during the further calcination with temperature increased to 550 °C at N<sub>2</sub> atmosphere [40]. The hollow structure of ZIF-67 after etching (Fig. 1d) induced the formation of more pore structures in carbon nitride, while the retained skeleton structure could adequately support carbon nitride and facilitated the shell collapse process. Meanwhile, the synthesized Co<sub>0.5</sub>Zn<sub>0.5</sub>-ZIF exhibited a prismatic dodecahedral structure (Fig. 1e), given its isoreticular properties and the similar lattice parameters of ZIF-67 (Co) and ZIF-8 (Zn) that made the bimetallic ZIF inherit the topology of both parent structures [41]. However, the average particle size of Co<sub>0.5</sub>Zn<sub>0.5</sub>-ZIF (average size of 0.21 μm) was barely half of the synthesized ZIF-67 (average size of 0.41 μm), which might be attributed to the decrease in the relative mole ratio of metal (Zn and Co) to dimethylimidazole that affected the nucleation process of ZIF and resulted in particle size reduction [42]. It has been reported that ZIF-8-derived porous carbon materials generally exhibit a microporous structure, large specific surface area, and high nitrogen doping level, while ZIF-67-derived carbon materials generally exhibited mesoporous structure and high graphitization but low specific surface area and N content [43–45]. As shown in Fig. 1f, the surface condensation of Co<sub>0.5</sub>Zn<sub>0.5</sub>-ZIF was much better than ZIF-67 after carbonization, attributed to the addition of Zn, which reduced the graphitization of the material surface. Moreover, the synthesized MCZC-10% exhibited a more significant porous structure (with the measured typical pore size being 236.4, 114.6, and 146.9 nm, Fig. 1g) than ZCCN-10% (with the measured typical pore size being 543.2, 433.1 and 264.7 nm, Fig. 1c). After etching with the same CA concentration for 3 h, more etching marks and opened facets (with the typical size of 59.1 and 66.7 nm)

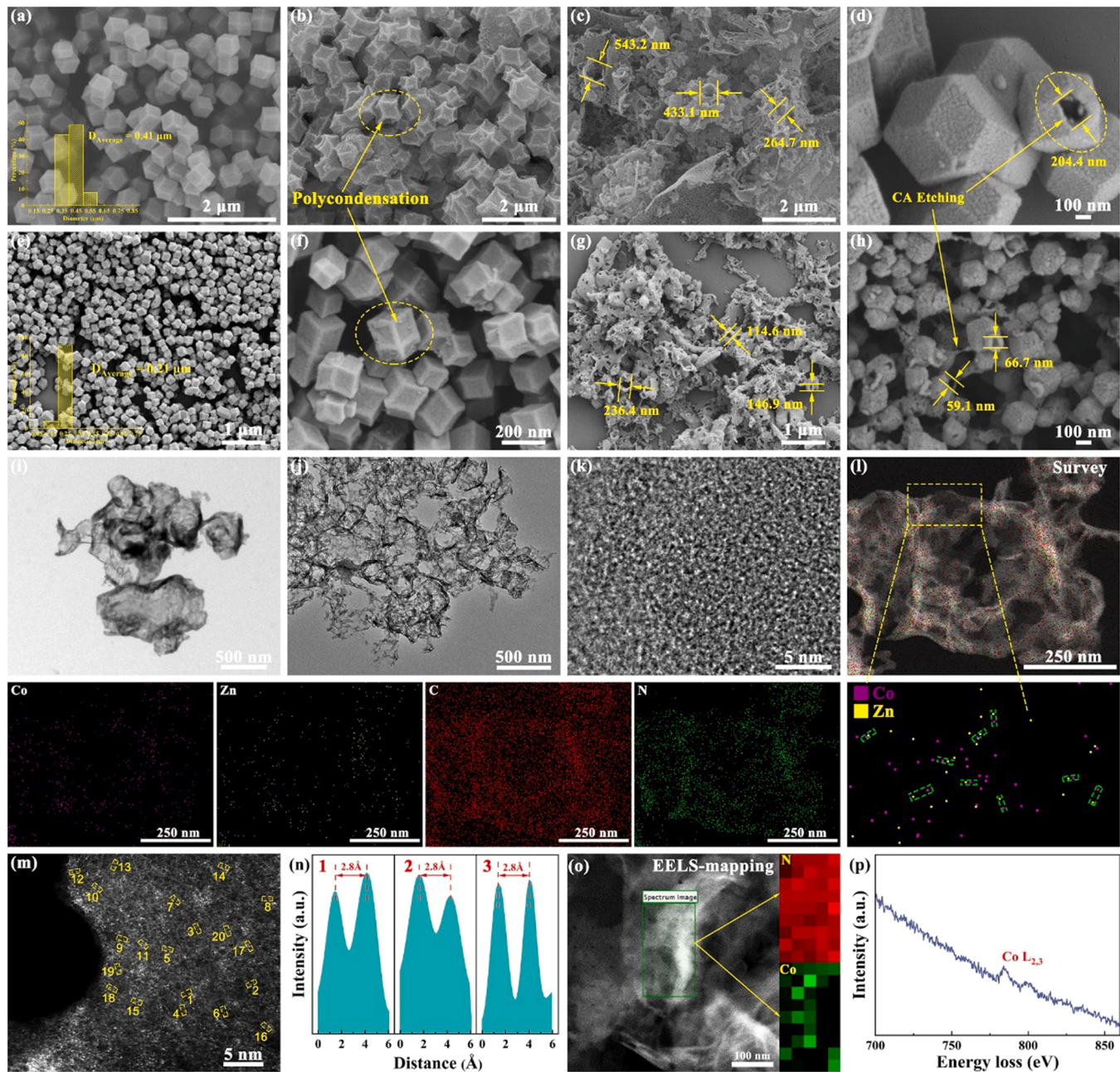


**Fig. 1.** SEM images of ZIF-67 (a), carbonized ZIF-67 (b), ZCCN-10% (c), and the etched ZIF-67 by CA for 3 h (d). SEM images of  $\text{Co}_{0.5}\text{Zn}_{0.5}$ -ZIF (e), carbonized  $\text{Co}_{0.5}\text{Zn}_{0.5}$ -ZIF (f), MCZC-10% (g), and the etched  $\text{Co}_{0.5}\text{Zn}_{0.5}$ -ZIF by CA for 3 h (h). TEM images of ZCCN-10% (i) and MCZC-10% (j). HR-TEM image of MCZC-10% (k). TEM-EDS mapping images of MCZC-10% (l) with the detailed distribution of the elements (Co, Zn, C, and N) exhibited separately. Aberration-corrected HAADF-STEM observation of MCZC-10% (m); Line-scanning intensity profiles obtained from the yellow region 1–3 in Fig. 1m (n); Atomic-resolution EELS mapping of Co and N (o); EELS spectra extracted from the atomic position highlighted in green in Fig. 1o (p).

were observed on  $\text{Co}_{0.5}\text{Zn}_{0.5}$ -ZIF (Fig. 1h). The hole size was much smaller than etching of ZIF-67 (with a typical size of 204.4 nm, Fig. 1d) since the relatively smaller size of  $\text{Co}_{0.5}\text{Zn}_{0.5}$ -ZIF provided more surfaces to etch and the slight difference in the atomic radius of Zn (1.39 Å) and Co (1.26 Å) led to instability of part of the bonds in Co-dimethylimidazole-Zn [46]. The TEM images of ZCCN-10% (Fig. 1i) and MCZC-10% (Fig. 1j) showed that the smaller size of  $\text{Co}_{0.5}\text{Zn}_{0.5}$ -ZIF and the better etching performance improved its unfolding at the 2-dimensional level, which helped solve the problem of condensation and agglomeration during the preparation of carbon nitride. And the hollow structure on MCZC-10% was further confirmed in Fig. S1. The  $\text{N}_2$  adsorption-desorption characterization of the synthesized catalysts showed that ZIF-67 ( $1473.5 \text{ m}^2 \cdot \text{g}^{-1}$ ,  $0.71 \text{ cm}^3 \cdot \text{g}^{-1}$ ) and  $\text{Co}_{0.5}\text{Zn}_{0.5}$ -ZIF

( $1317.0 \text{ m}^2 \cdot \text{g}^{-1}$ ) exhibited similar  $S_{\text{BET}}$  and pore volumes, but the pore size of  $\text{Co}_{0.5}\text{Zn}_{0.5}$ -ZIF (19.70 nm) was significantly larger than that of ZIF-67 (4.86 nm). After the carbonization of  $\text{Co}_{0.5}\text{Zn}_{0.5}$ -ZIF, a relatively large  $S_{\text{BET}}$ , pore size, and pore diameter ( $347.7 \text{ m}^2 \cdot \text{g}^{-1}$ ,  $0.25 \text{ cm}^3 \cdot \text{g}^{-1}$ , and 13.13 nm) were maintained for the newly formed ZIF-8-like structure with Zn as the metal site, which helped to form larger  $S_{\text{BET}}$  than ZCCN-10% with relatively large pore volume and pore capacity as well (Fig. S2 and Table S1). This phenomenon facilitated the exposure of catalytic sites and accelerated PMS activation rate, consistent with SEM and TEM characterizations. No surface particles or crystallite structure attributed to Co or Zn oxides or carbides were observed in the High-Resolution Transmission Electron Microscopy (HRTEM) image of MCZC-10% (Fig. 1k), which precluded the formation of crystalline metal

species. TEM-EDS mapping of MCZC-10% (Fig. II with detailed element distribution) exhibited a high dispersion of Co, Zn, C, and N and clear atom pairs of Co and Zn (typically circled by green boxes). Considering the accuracy of TEM-EDS, the aberration-corrected high-angle annular dark-field scanning transmission electron microscopy (AC-HAADF-STEM) was used to further investigate the Co and Zn distribution state. As shown in Fig. 1m, metal sites exhibited a clear isolated distribution and many bright spots in pairs (typically circled by yellow boxes). The distances of atom pairs identified by the intensity profiles in the 20 randomly selected regions were close to  $\sim 2.8$  Å (Fig. 1m, n), which indicated the formation of pairs of Co and Zn. Furthermore, the atomic-resolution electron energy-loss spectroscopy (EELS) line-scan showed that all analyzed atom pairs contained Co and N atoms. Although the poor response of EELS to Zn resulted in the inability to capture the signal of Zn in EELS mapping (Fig. 1o, p), the combination with the signal of Zn captured in TEM-EDS and the absence response region around the Co sites in EELS-mapping implied the formation of heteroatom Co-Zn pairs in MCZC-10%.

The physical phase structure of the synthesized catalysts was further analyzed based on XRD patterns. As shown in Fig. S3a, XRD patterns of the synthesized  $\text{Co}_{0.5}\text{Zn}_{0.5}$ -ZIF were consistent with ZIF-67 and ZIF-8, with the peaks corresponding to (002), (112), (022), (013) and (222) crystal planes, respectively [47]. This finding indicated no adverse influence on the original prismatic dodecahedral structure, consistent with the SEM characterization results. No diffraction peaks were observed on the carbonized  $\text{Co}_{0.5}\text{Zn}_{0.5}$ -ZIF, and only one broad peak centered at  $\sim 27.4^\circ$  corresponding to (002) crystal plane of carbon nitride was

observed on the XRD patterns of MCZC catalyst (Fig. S3b) with severely decreased intensity of the initial peak at  $\sim 13.1^\circ$  corresponding to the (100) crystal plane compared with the synthesized PCN, indicating the formation of Co-N and Zn-N bonds [48]. With an increase in  $\text{Co}_{0.5}\text{Zn}_{0.5}$ -ZIF, the intensity of diffraction peaks attributed to the (002) crystal plane of carbon nitride gradually decreased, which is attributed to the increase of Co-N and Zn-N coordination bonds anchored in the two-dimensional molecular system of carbon nitride further disrupting the inherent alignment period of its molecular structure (Fig. S3c) [49]. The Raman spectra of MCZC-10% and PCN (Fig. S3d) exhibited two obvious peaks attributing to the D band and G band at  $1342\text{ cm}^{-1}$  and  $1590\text{ cm}^{-1}$  with the higher  $I_D/I_G$  of MCZC-10% (1.1) than that of PCN (1.04) after the doping of Co and Zn, indicating the successful anchoring of metal atoms and the generation of defects and imperfections [50]. Consistent findings were found in the FTIR spectra of the synthesized MCZC catalysts (Fig. S4a) with decreased intensity of the peaks attributed to N-(C3) and C=N-C near  $1334\text{ cm}^{-1}$  and  $1251\text{ cm}^{-1}$  with an increase of  $\text{Co}_{0.5}\text{Zn}_{0.5}$ -ZIF since the interaction of Co/Zn metal atoms with N atoms on PCN could affect the stretching vibration of aromatic heterocycles [51]. Meanwhile, the intensity of absorption vibrational peak attributed to the N-H bond at  $3209\text{ cm}^{-1}$  decreased with an increase in Co and Zn atoms exposed, forming more Co-N and Zn-N bonds on the PCN array that led to a decrease in the charge density of N atoms [42], consistent with XRD results. This finding confirmed the formation of Co-N and Zn-N bonds. Interestingly, no absorption vibration peak attributed to water molecules near  $3500\text{ cm}^{-1}$  on the spectrum of  $\text{Co}_{0.5}\text{Zn}_{0.5}$ -ZIF was observed, while there was a clear peak at a similar

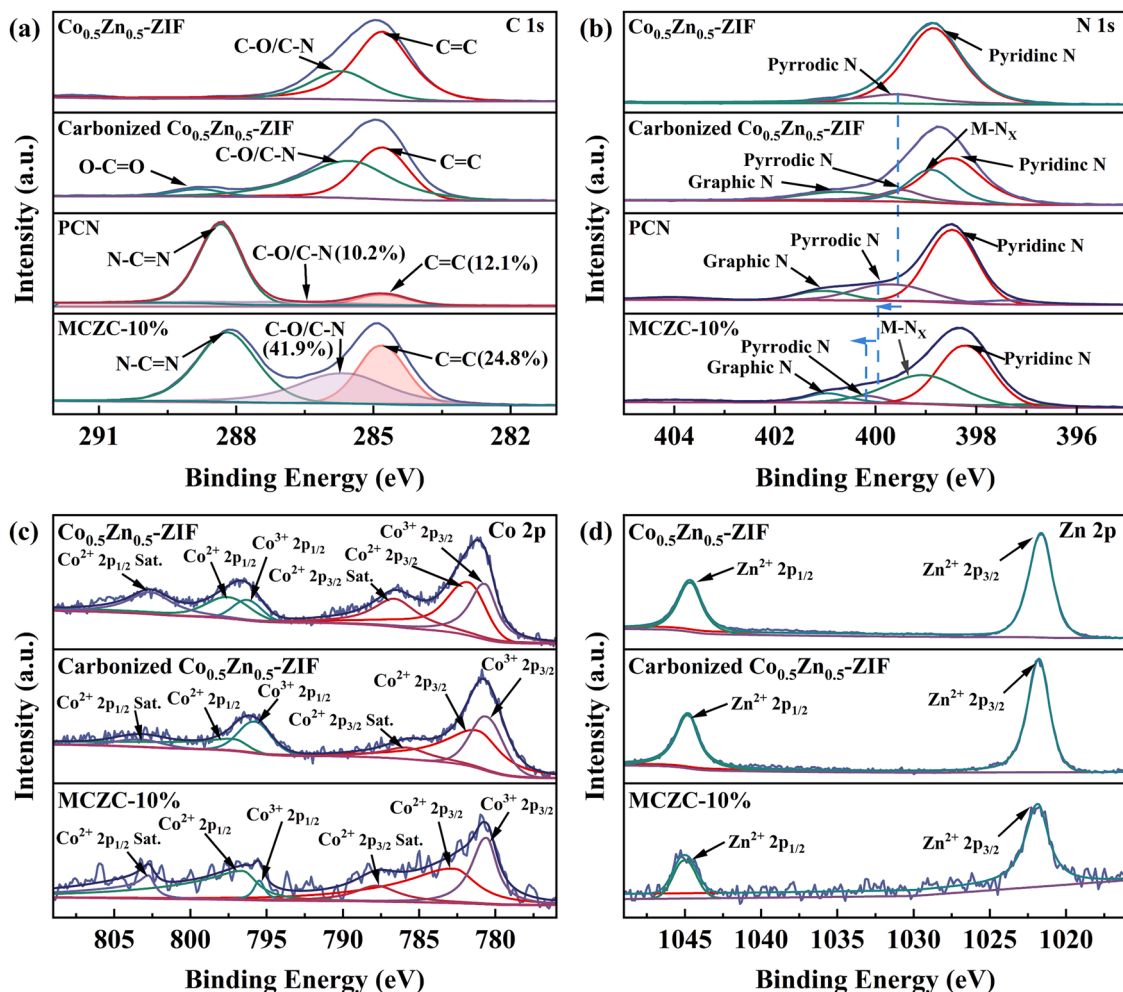


Fig. 2. XPS spectra of the synthesized catalysts: C 1 s (a); N 1 s (b); Co 2 p (c); Zn 2 p (d).

position on the spectrum of ZIF-67 (Fig. S4b), which might be attributed to the formation of ZIF-8-like structures that retained the hydrophobic properties of ZIF-8 [52].

XPS characterizations were further conducted to clarify the surface composition and chemical state of the synthesized MCZC catalyst. As shown in Fig. S5a, the survey spectrum of MCZC-10% confirmed the presence of Co, Zn, C, N, and O, with the content of Co and Zn being 0.42 and 0.53 at% (Table S2), respectively. The peaks around 284.8, 285.9, and 288.2 eV on the high-resolution C 1 s spectra of the synthesized catalysts were attributed to the C=C, C–O/C–N, and N–C=N bonds, respectively (Fig. 2a) [53]. Compared with PCN, the area of the peak attributed to C=C bonds on MCZC-10% increased from 12.1% to 24.8%, facilitating electron transfer [54]. The peaks around 398.3 and 400.1 eV on the high-resolution N 1 s spectra (Fig. 2b) of the synthesized catalysts were attributed to the pyrrole N and pyridine N [55]. The abundance of pyridine N on catalyst could facilitate the formation of Metal-N<sub>x</sub> bonds by anchoring metal atoms (~399.2 eV), while graphite N (~ 401.2 eV) could enhance the electron transfer properties of carbon materials [56]. The high-resolution Co 2p spectrum (Fig. 2c) of MCZC-10% confirmed the coexistence of Co<sup>2+</sup> and Co<sup>3+</sup> with peaks at 780.8, 782.9, 795.5, 796.6, 787.8 and 802.5 eV attributed to Co<sup>3+</sup> 2p<sub>3/2</sub>, Co<sup>2+</sup> 2p<sub>3/2</sub>, Co<sup>3+</sup> 2p<sub>1/2</sub>, Co<sup>2+</sup> 2p<sub>1/2</sub> and the satellite peaks of Co<sup>2+</sup> 2p<sub>3/2</sub> and Co<sup>2+</sup> 2p<sub>1/2</sub> [57]. The high-resolution Zn 2p spectrum (Fig. 2d) of MCZC-10% confirmed the presence of Zn<sup>2+</sup> with peaks at 1023 and 1045 eV attributed to Zn<sup>2+</sup> 2p<sub>3/2</sub> and Zn<sup>2+</sup> 2p<sub>1/2</sub> with clear characterization of Zn<sup>2+</sup> in the Osher energy spectrum (Fig. S5b) [58]. No peaks attributed to metal oxides of Co or Zn were observed in the high-resolution O 1 s spectra of the synthesized catalyst (Fig. S5c), with both peaks at 532.1

and 531.3 eV attributed to C–O bonds and peaks at 532.8 eV and 533.8 eV attributed to C=O and O–H bonds, respectively [48], which further validated successful doping of Co and Zn.

### 3.2. Catalytic performance of the MCZC catalyst

A series of experiments were conducted to investigate the performance of the synthesized catalysts on PMS activation for TC degradation. As shown in Fig. 3a, no efficient TC degradation could be achieved by PMS autolysis, and the highest TC adsorption efficiency (equilibrium) achieved by MCZC-10% was only 9.8% within 30 min, indicating that adsorption was not the main contributor to TC removal. Compared with ZCCN-10%, the TC degradation efficiency was significantly improved from 74.9% to 99.6%, with the degradation constant  $k_{\text{obs}}$  increased from  $0.056 \text{ min}^{-1}$  to  $0.228 \text{ min}^{-1}$  within 24 min, which was attributed to the coordination of Co and Zn atoms. After increasing the dosage of  $\text{Co}_{0.5}\text{Zn}_{0.5}\text{-ZIF}$  from 10% to 20%, the TC degradation efficiency slightly decreased from 99.6% to 95.7% ( $k_{\text{obs}}$  decreased from  $0.228 \text{ min}^{-1}$  to  $0.12 \text{ min}^{-1}$ ) within 24 min (Fig. S6a), related to the large addition of  $\text{Co}_{0.5}\text{Zn}_{0.5}\text{-ZIF}$  that consumed a large amount of CA and negatively affected the formation of porous structure, resulting in the loss of  $S_{\text{BET}}$  and the ineffective distribution of Co and Zn atoms in local agglomerates [30]. Moreover, when the catalyst dose was further increased from  $0.2 \text{ g}\cdot\text{L}^{-1}$  to  $0.3 \text{ g}\cdot\text{L}^{-1}$ , no significant improvement in the TC degradation efficiency was observed (Fig. S6b) when the  $k_{\text{obs}}$  increased from  $0.228 \text{ min}^{-1}$  to  $0.254 \text{ min}^{-1}$  since the excessive MCZC-10% could quench  $\text{SO}_4^{2-}$  [59]. TC degradation efficiency significantly decreased from 99.6% to 85.7% ( $k_{\text{obs}}$  decreased from  $0.255 \text{ min}^{-1}$  to  $0.08 \text{ min}^{-1}$ )

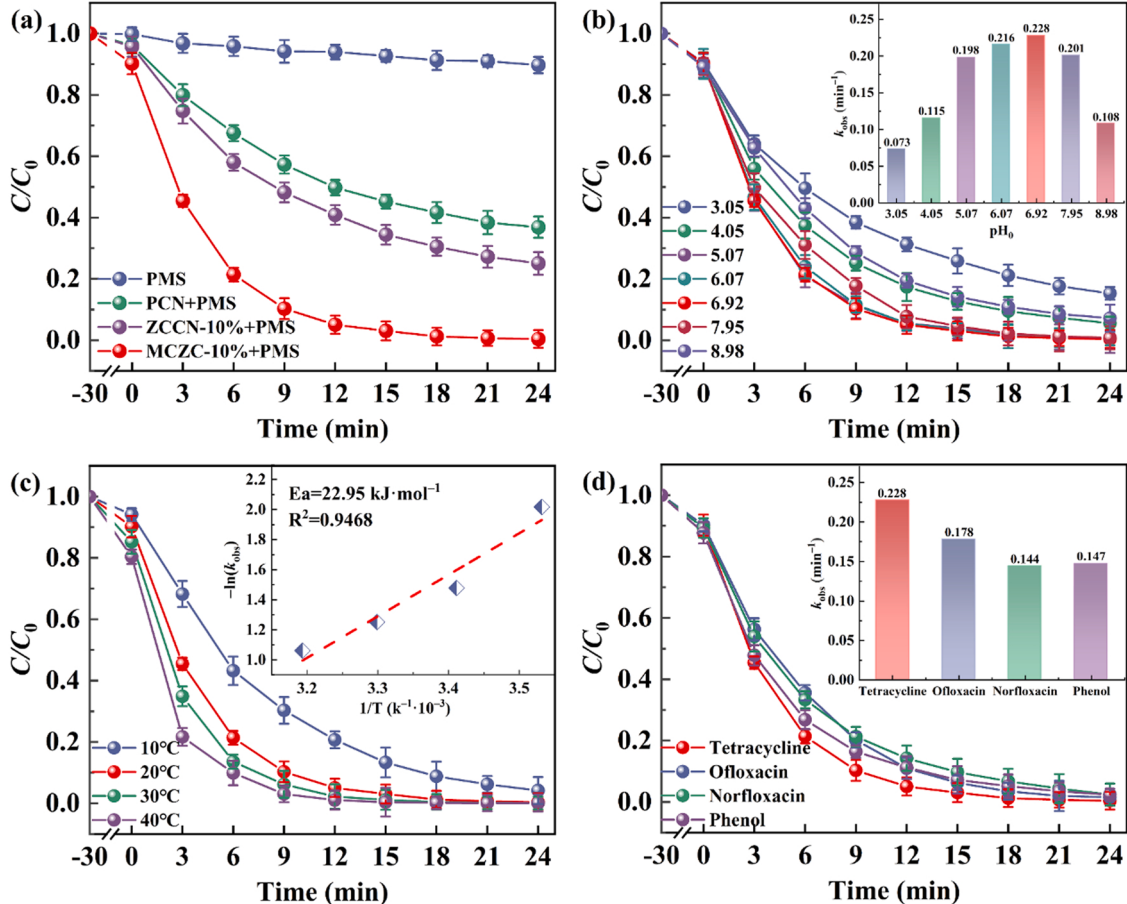


**Fig. 3.** Influences of different systems (a), pH (b) and temperature (c) on TC degradation performance. The degradation of different pollutants by MCZC-10% (d). (Except the exact analyzing factor, other factors were fixed with catalyst dosage =  $0.2 \text{ g} \cdot \text{L}^{-1}$ , PMS = 1 mM, TC concentration =  $10 \text{ mg} \cdot \text{L}^{-1}$ , pH = 7, temperature =  $20^\circ\text{C}$ ).

with the initial TC concentration increased from 5 mg·L<sup>-1</sup> to 40 mg·L<sup>-1</sup>, which was attributed to the limited generation of active radicals with fixed PMS concentration and catalyst dosage, wherein a higher ratio of radicals to TC would bring greater degradation performance [60]. The increase of PMS concentration from 1 mM to 2 mM could not significantly enhance the TC degradation efficiency as the  $k_{\text{obs}}$  only increased from 0.228 min<sup>-1</sup> to 0.236 min<sup>-1</sup> (Fig. S6d). Partly, the limited number of Co sites could not simultaneously adsorb more PMS to active them. On the other hand, the excess PMS would react with SO<sub>4</sub><sup>2-</sup> and HO<sup>•</sup> to form other active species with lower oxidation potential, thus inhibiting the further improvement of TC degradation (Eqs. S4–S7) [61]. The theoretical stoichiometric PMS dosage for complete oxidation of TC (10 mg·L<sup>-1</sup>) was calculated to be 2.3 mM by Eq. S8 [62]. However, the increase of PMS dosage from 1 mM to 2.3 mM only increased the TOC removal efficiency from 55.8% to 57.1% (Fig. S6e), which reflected the economy and efficiency of the optimal PMS dosage of 1 mM in MCZC-10%/PMS system for TC degradation, with the PMS dosage well below the stoichiometry.

The influence of initial pH on TC degradation was further investigated. As shown in Fig. 3b, the TC degradation efficiency decreased from 99.6% to 84.7% ( $k_{\text{obs}}$  decreased from 0.228 min<sup>-1</sup> to 0.073 min<sup>-1</sup>) within 24 min when the initial pH decreased from 6.92 to 3.05, which might be attributed to the increase of H<sup>+</sup> concentration that suppressed PMS adsorption on Co sites and helped stabilize PMS to limit the activation process [63,64]. In addition, the leached amount of Co and Zn increased from 9.3 and 9.6 µg·L<sup>-1</sup> to 25.6 and 27.5 µg·L<sup>-1</sup>, with the initial pH decreasing from 6.92 to 3.05 (Fig. S7a). Although this would bring little secondary aquatic environmental risk, the loss of active components caused a reduction in catalytic performance. In contrast, although the leaching of Co and Zn under alkaline conditions was limited, the TC degradation efficiency still decreased from 99.6% to 92.8% ( $k_{\text{obs}}$  decreased from 0.228 min<sup>-1</sup> to 0.108 min<sup>-1</sup>) within 24 min. At a pH > 7.6, PMS mainly existed as SO<sub>5</sub><sup>2-</sup> rather than HSO<sub>5</sub><sup>-</sup> (Fig. S7b), which increased its affinity for HO<sup>•</sup> to generate S<sub>2</sub>O<sub>8</sub><sup>2-</sup> and further quenched the generated SO<sub>4</sub><sup>2-</sup> (Eqs. S8–S9). Meanwhile, the generated SO<sub>4</sub><sup>2-</sup> could react with OH<sup>-</sup> or H<sub>2</sub>O to generate HO<sup>•</sup> with lower oxidation potential than SO<sub>4</sub><sup>2-</sup> and further suppress TC degradation (Eqs. S10–S11) [65]. Moreover, the different forms of TC (Fig. S7c) and the variety of surface charges of MCZC-10% (Fig. S7d) under different pHs could affect TC removal efficiency. The pH<sub>pzc</sub> (zero charge) of MCZC-10% was 4.45. At a pH < 3.1, an electrostatic repulsion was found between MCZC-10% and TC, given that TC mainly existed as TCH<sub>3</sub><sup>+</sup> and the surface charge of MCZC-10% was positive. At a pH > 7.9, an electrostatic repulsion was found between MCZC-10% and TC since TC mainly existed in the form of TCH<sup>-</sup> and TC<sup>2-</sup> and the surface charge of MCZC-10% was negative. At a pH ranging from 3.1 to 7.9, there might exist an electrostatic attraction since TC mainly existed in the form of TCH<sub>2</sub><sup>0</sup> and the surface discharge of MCZC-10% was positive at pH 3.1–4.45 and negative at pH 4.45–7.9; however, poor adsorption performance of MCZC-10% was observed for TC removal, indicating the removal of TC mainly relied on the catalytic process rather than adsorption. In addition, unlike the strong zeta potential close to -40 mV observed at pH 5–9, the highest zeta potential at pH 3 and 4 was only 25.3 mV, indicating instability of MCZC-10% under acidic conditions and good stability under weak acidic and neutral conditions. Influences of the leached Co and Zn (at pH = 6.9) on TC degradation were further investigated and the result exhibited almost no activation of PMS for TC degradation because of the extremely low concentration of Co (II), indicating little influence to the accurate identification of catalytic performance of MCZC-10% (Fig. S7e). The calculated catalytic activation energy ( $E_a$ ) of MCZC-10% was 22.95 kJ·mol<sup>-1</sup> (Fig. 3c), which was much higher than that of diffusion-controlled reactions (10–13 kJ·mol<sup>-1</sup>), revealing that the quick PMS activation to the generation of active species over MCZC-10% catalyst were the key for TC degradation rather than mass transfer [66]. And the relatively lower  $E_a$  on MCZC-10% exhibited the higher catalytic activity as compared to that of FCOCN2 (23.88 kJ·mol<sup>-1</sup>) [60],

Co@MoS<sub>2</sub> (27.5 kJ·mol<sup>-1</sup>) [57], and hollow Fe-MFI zeolite (40.24 kJ·mol<sup>-1</sup>) [67] in PMS activation for TC degradation. The efficient degradation of ofloxacin (98.4%,  $k_{\text{obs}}$  of 0.178), norfloxacin (97.6%,  $k_{\text{obs}}$  of 0.144), and phenol (97.7%,  $k_{\text{obs}}$  of 0.147) within 24 min by MCZC-10%/PMS indicated the excellent catalytic and non-selective properties of the catalyst. The detailed pseudo-first-order kinetic fittings of the above investigations are shown in Fig. S8.

### 3.3. Influences of inorganic ions and NOMs

The influence of common inorganic ions (Cl<sup>-</sup>, SO<sub>4</sub><sup>2-</sup>, NO<sub>3</sub><sup>-</sup>, H<sub>2</sub>PO<sub>4</sub><sup>-</sup> and CO<sub>3</sub><sup>2-</sup>) and HA (a typical one among NOMs) on TC degradation were systematically investigated. As shown in Fig. 4a, the performance of MCZC-10% on TC degradation was slightly increased with  $k_{\text{obs}}$  increased from 0.228 min<sup>-1</sup> to 0.310 min<sup>-1</sup> by 20 mM of Cl<sup>-</sup>. Although SO<sub>4</sub><sup>2-</sup> were quenched by Cl<sup>-</sup> through one-electron abstraction from Cl<sup>-</sup> (SO<sub>4</sub><sup>2-</sup> + Cl<sup>-</sup> → Cl<sup>•</sup> + SO<sub>4</sub><sup>2-</sup>), the considerable concentration of Cl<sup>-</sup> maintained the co-existence of Cl<sup>•</sup>, Cl<sub>2</sub><sup>-</sup> (Cl<sup>•</sup> + Cl<sup>-</sup> → Cl<sub>2</sub><sup>-</sup>) and OCl<sup>•-</sup>. And the further reactions involving Cl<sup>•</sup> and Cl<sub>2</sub><sup>-</sup> led to the formation of Cl<sub>2</sub> (Cl<sup>•</sup> + Cl<sub>2</sub><sup>-</sup> → Cl<sub>2</sub> + Cl<sup>-</sup>; Cl<sub>2</sub><sup>-</sup> + Cl<sup>•</sup> → Cl<sub>2</sub> + 2Cl<sup>-</sup>) and HOCl (Cl<sub>2</sub> + H<sub>2</sub>O → HOCl + Cl<sup>-</sup> + H<sup>+</sup>; Cl<sup>-</sup> + HSO<sub>5</sub><sup>-</sup> → SO<sub>4</sub><sup>2-</sup> + HOCl). The relatively high standard reduction potentials of Cl<sup>•</sup>/Cl<sup>-</sup> (2.5 V<sub>NHE</sub>), Cl<sub>2</sub><sup>-</sup>/Cl<sup>-</sup> (2.2 V<sub>NHE</sub>) and HOCl (with a much longer life time) would help enhancing the TC degradation since those radicals were widely acknowledged to efficiently react with the electron-rich organics [68–70]. No significant inhibitory effect of SO<sub>4</sub><sup>2-</sup> and NO<sub>3</sub><sup>-</sup> on TC degradation was observed (Fig. 5b and c) since SO<sub>4</sub><sup>2-</sup> could shorten the attack path of SO<sub>4</sub><sup>2-</sup> on TC, and NO<sub>3</sub><sup>-</sup> could induce the generation of O<sup>•</sup> to further attack TC [71,72]. CO<sub>3</sub><sup>2-</sup> exhibited an inhibitory effect on TC degradation since CO<sub>3</sub><sup>2-</sup> could not only raise the pH to reduce the amount of HSO<sub>5</sub><sup>-</sup> with higher oxidation potential but was easily converted to HCO<sub>3</sub><sup>-</sup> to quench HO<sup>•</sup> [73]. The slightly enhanced TC degradation performance by H<sub>2</sub>PO<sub>4</sub><sup>-</sup> was mainly attributed to the asymmetry of the PMS molecular structure that made H<sub>2</sub>PO<sub>4</sub><sup>-</sup> capable of interacting with the PMS to reduce the dissociation energy of the O–O bond, thus accelerating the PMS activation process [74]. 10 mg·L<sup>-1</sup> of HA slightly attenuated the TC degradation efficiency from 99.6% to 91% ( $k_{\text{obs}}$  decreased from 0.228 min<sup>-1</sup> to 0.098 min<sup>-1</sup>) within 24 min, given that HA could quench the generated active species, which revealed the efficient and stable catalytic performance of MCZC-10% despite the interference of HA [75]. To further identify the application prospect of MCZC-10% in natural water bodies, water samples from the Jiajiang River (close to Nanjing Chemical Industry Park) and Yangtze River were selected as water matrix investigation subjects (detailed water quality parameters and location of the two sources shown in Fig. 4b). As shown in Fig. 4c, the TC degradation performance in tap water slightly decreased to 99.2% ( $k_{\text{obs}}$  to 0.207 min<sup>-1</sup>), indicating the efficient performance of MCZC-10%/PMS under the influences of the possible existence of Na<sup>+</sup>, Ca<sup>2+</sup>, Mg<sup>2+</sup>, Fe<sup>3+</sup>, HCO<sub>3</sub><sup>-</sup>, Cl<sup>-</sup>, and SO<sub>4</sub><sup>2-</sup> in tap water. Besides, the TC degradation performance in Jiajiang River and Yangtze River slightly decreased to 90.8% ( $k_{\text{obs}}$  decreased of 0.120 min<sup>-1</sup>) and 94.9% ( $k_{\text{obs}}$  of 0.094 min<sup>-1</sup>), which might be attributed to the interference from other containments (NOMs, organics, bacteria, etc.). Despite the efficiency reduction, the MCZC-10%/PMS still maintained a high TC degradation efficiency (over 90%), indicating its potential for practical application. Detailed information on the influence of inorganic ions, HA, and water matrix and their corresponding pseudo-first-order kinetic fittings on TC degradation are shown in Fig. S9.

### 3.4. Catalytic mechanism of MCZC catalyst

Radical quenching experiments were conducted to identify the active species participating in TC degradation and their corresponding contributions with p-BQ, TBA, EtOH, AgNO<sub>3</sub>, and L-His/FFA as quenchers of O<sub>2</sub><sup>•-</sup>, HO<sup>•</sup>, HO<sup>•</sup>/SO<sub>4</sub><sup>2-</sup>, electron and <sup>1</sup>O<sub>2</sub> [76]. As shown in Fig. 5a, excess TBA inhibited TC degradation by 4%, indicating the participation of

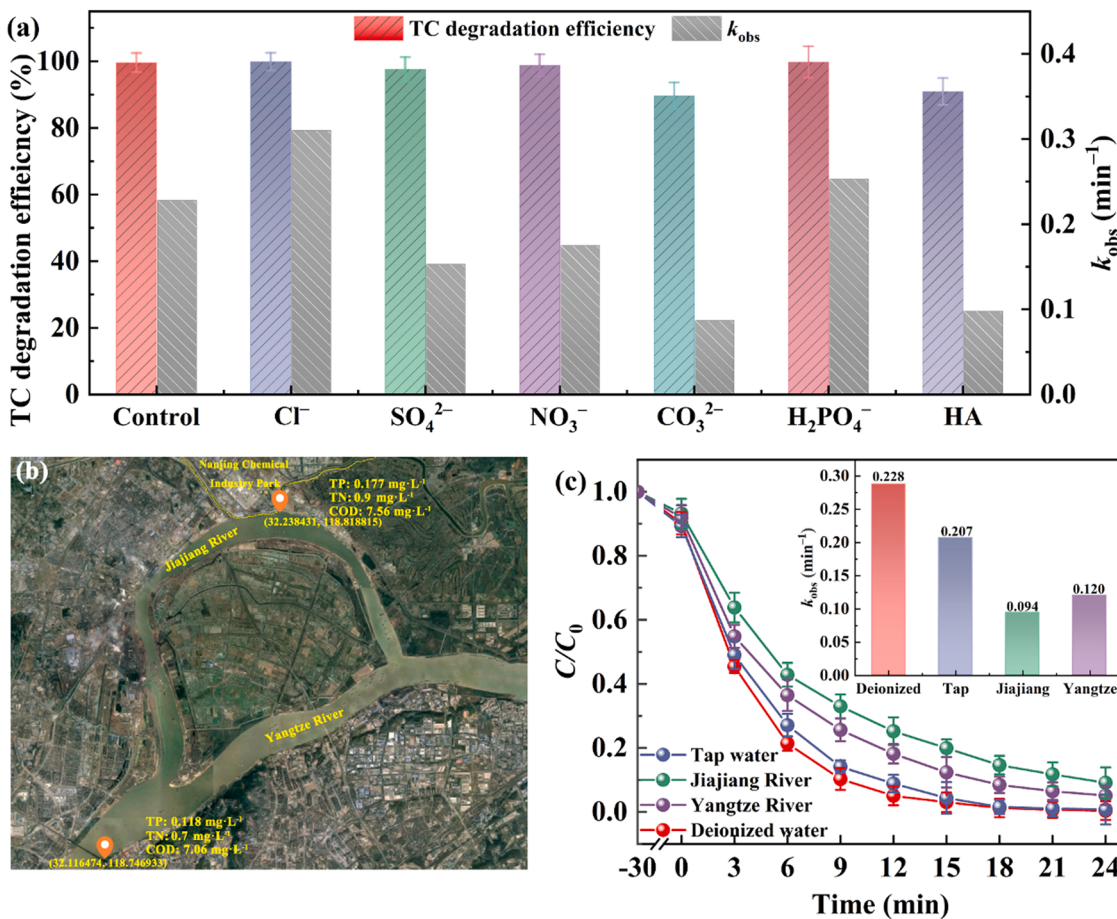


**Fig. 4.** Influences of inorganic ions and HA on TC degradation over MCZC-10% with the concentrations of inorganic ion and HA being 20 mM and 10 mg·L<sup>-1</sup> respectively (a); Water quality parameters and the sampling location for water matrix experiment (b); Influences of different water sources on TC degradation in MCZC-10%/PMS system (c). (Except the exact analyzing factor, other factors were fixed with catalyst dosage = 0.2 g·L<sup>-1</sup>, PMS = 1 mM, TC concentration = 10 mg·L<sup>-1</sup>, pH = 7, temperature = 20 °C).

HO<sup>•</sup>, although it was not the major contributor. In contrast, excess EtOH inhibited TC degradation by 21.4%, suggesting a more significant contribution of SO<sub>4</sub><sup>2-</sup> than HO<sup>•</sup>. The participation of O<sub>2</sub><sup>•-</sup> and <sup>1</sup>O<sub>2</sub> were confirmed by the inhibition of TC degradation efficiency by 12.9% and 49.8%, with *p*-BQ and *L*-His as scavengers, respectively. Considering that *L*-His might lead to the rapid decomposition of PMS to amplify the contribution of <sup>1</sup>O<sub>2</sub> [77], FFA was further selected as a comparative scavenger of <sup>1</sup>O<sub>2</sub> and the TC degradation was inhibited by 39.7%, which further confirmed the main contribution of <sup>1</sup>O<sub>2</sub> to TC degradation. Moreover, <sup>1</sup>O<sub>2</sub> was revealed to be generated by PMS decomposition since the solution was aerated with excess N<sub>2</sub> for 40 min to eliminate the effect of dissolved oxygen [78]. It has been reported that the generation of ROS is inherently initiated by one-electron reduction of PMS, hence, AgNO<sub>3</sub> was selected as the scavenger of electron due to its high performance on quenching electrons but poor performance with PMS activation. The result revealed an interesting finding that the TC degradation was not inhibited but improved ( $k_{obs}$  increased from 0.228 min<sup>-1</sup> to 0.265 min<sup>-1</sup>) with excess AgNO<sub>3</sub>, which was mainly attributed to the efficient electron transfer on MCZC-10% that efficiently prevented AgNO<sub>3</sub> from annihilating electrons [79]. However, there might be a situation that the Ag<sup>+</sup> would capture an electron to form Ag<sup>0</sup>, which could be deposited on the surface of MCZC-10% to enhance the electron transfer process and cause controversial identification of mediated electron transfer. Hence, further investigations of the mediated electron transfer were performed. As shown in Fig. S10a, comparing with segment 1, a new anodic peak appeared in segment 2 and 3 and the current intensity of the cathodic peak decreased as the

number of scanning cycles increased due to the generation of oxidation of FFA and the aggregation of the intermediates at the electrode, indicating that FFA could be oxidized by mediate electron transfer and it was an irreversible system [80]. This was further confirmed as an instantaneous current intensity observed after the FFA addition (Fig. S10b). Besides, the FFA degradation by MCZC-10%/PMS system was further performed and the result exhibited 22.8% degradation efficiency of FFA within 24 min (Fig. S10c), indicating the possible direct oxidation by mediated electron transfer. Basing on the quenching experiment, the inhibition rate of  $k_{obs}$  by different scavengers was calculated and the contributions of the corresponding active radicals was listed as follows: <sup>1</sup>O<sub>2</sub> > SO<sub>4</sub><sup>2-</sup> > O<sub>2</sub><sup>•-</sup> > HO<sup>•</sup> (Fig. 5b), which indicated that TC degradation was a non-radical-mediated process. Detailed information on the influence of different scavengers and their corresponding pseudo-first-order kinetic fittings on TC degradation are shown in Fig. S11.

The possible formation of high-valence Co-oxo species in MCZC-10%/PMS system was investigated with DMSO as the scavenger. As shown in Fig. S10d, no peaks attributing to DMSO<sub>2</sub> at 197 nm was observed in the UV-vis spectra of DMSO/MCZC-10%/PMS system within 12 min and the intensity of the peak attributing to DMSO at 207 nm slightly decreased due to the attack from SO<sub>4</sub><sup>2-</sup> and HO<sup>•</sup> [81], which was corresponded to the DMSO quenching experiment that the TC degradation efficiency slightly decreased from 99.6% to 95.2% (Fig. S10e-f) with DMSO concentration increased from 0 to 100 mM. These results demonstrated the negligible formation of high-valent Co-oxo species in MCZC-10%/PMS system.

Further evidence of the identified ROS was provided by EPR analysis

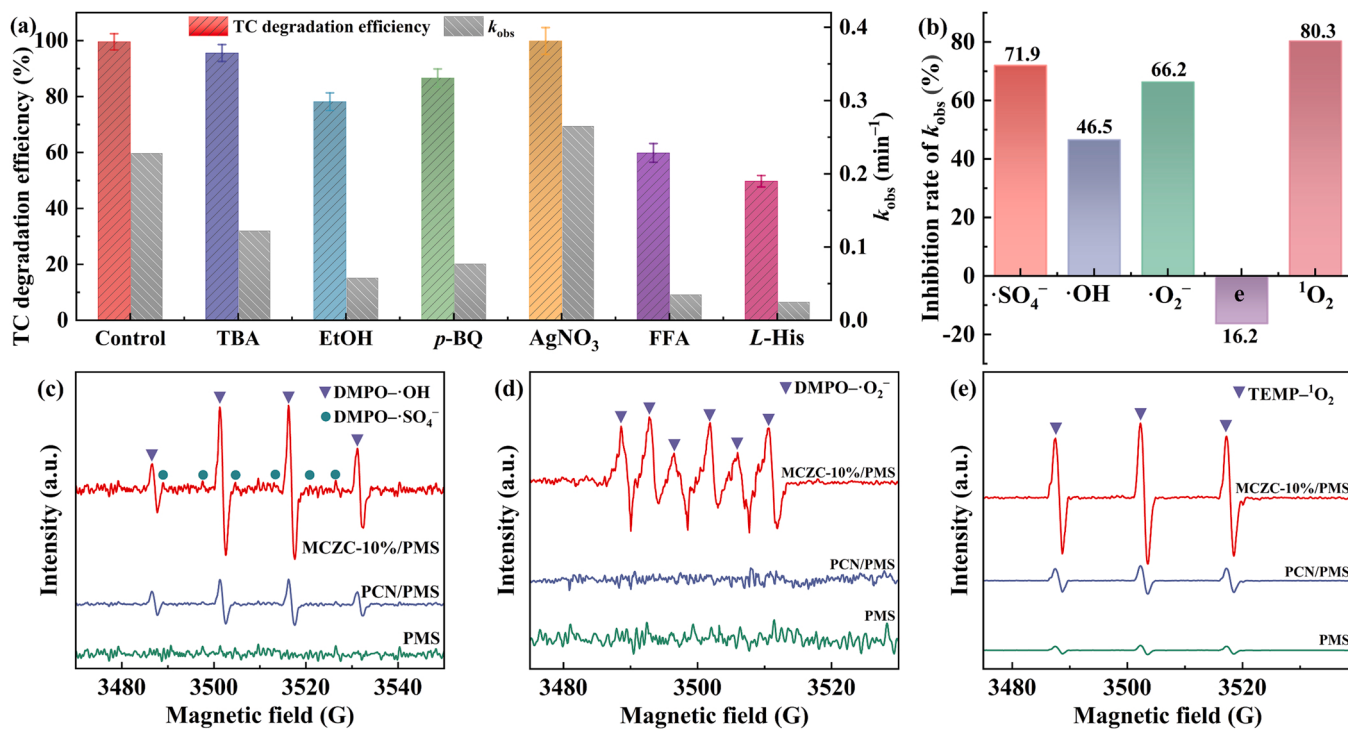


**Fig. 5.** Influences of overdosed different scavengers on TC degradation over MCZC-10% (a); Inhibition rate of  $k_{\text{obs}}$  by different radicals (b) (Inhibition rate of  $k_{\text{obs}}$  (%) =  $1 - k_{\text{obs}}/k_{\text{obs}}$ ); EPR spectra of DMPO- $\text{SO}_4^-$  and DMPO- $\text{HO}^*$  (c), DMPO- $\text{O}_2^-$  (d) and TEMP- $^1\text{O}_2$  (e).

with DMPO and TEMP as the spin trapping agents. As shown in Fig. 5c, clear signals attributed to DMPO- $\text{SO}_4^-$  (six peaks) and DMPO- $\text{HO}^*$  (1:2:2:1) were captured in both PCN/PMS and MCZC-10%/PMS systems with the intensity of the latter being relatively stronger, indicating

MCZC-10% catalysis was promoted to generate  $\text{SO}_4^-$  and  $\text{HO}^*$  [82]. Signals attributed to DMPO- $\text{O}_2^-$  were only captured in MCZC-10%/PMS (Fig. 5d) for the catalytic activation of Co sites. No obvious signals attributed to DMPO- $\text{SO}_4^-$ , DMPO- $\text{HO}^*$ , and DMPO- $\text{O}_2^-$  were captured

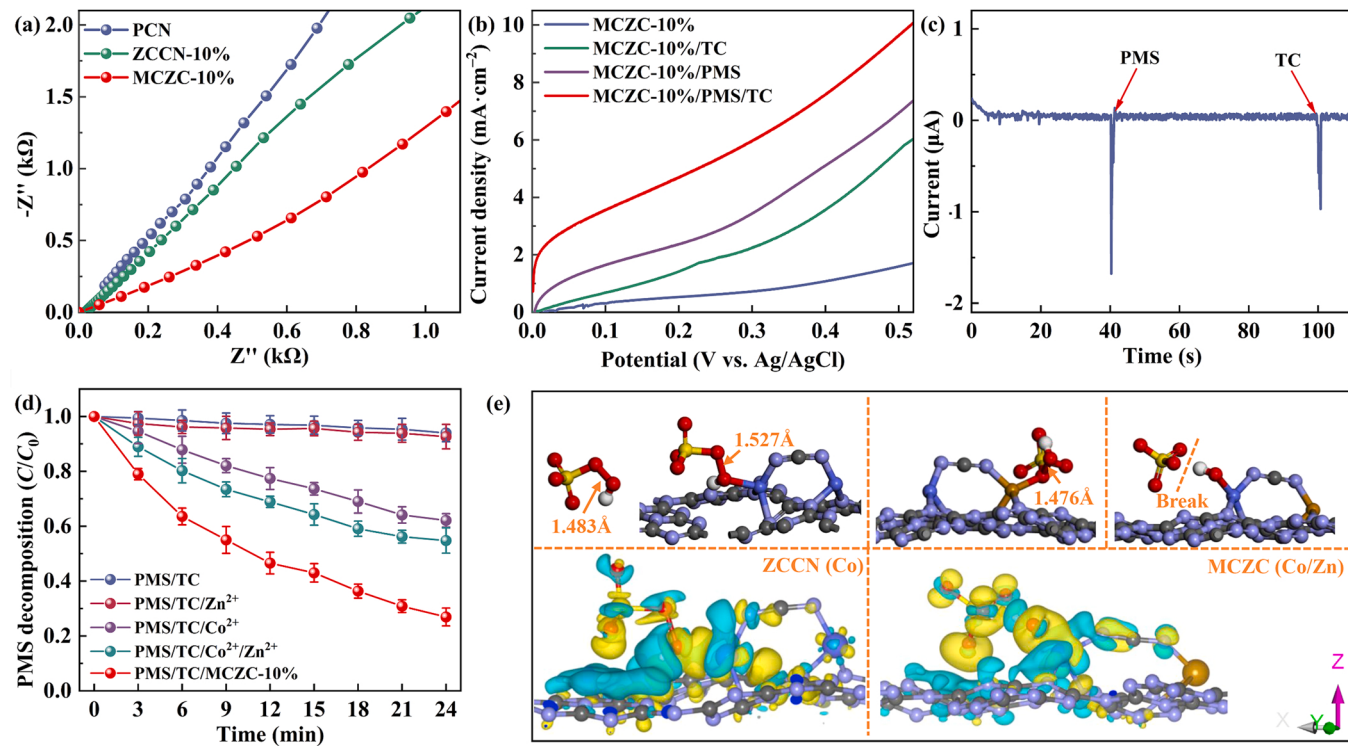


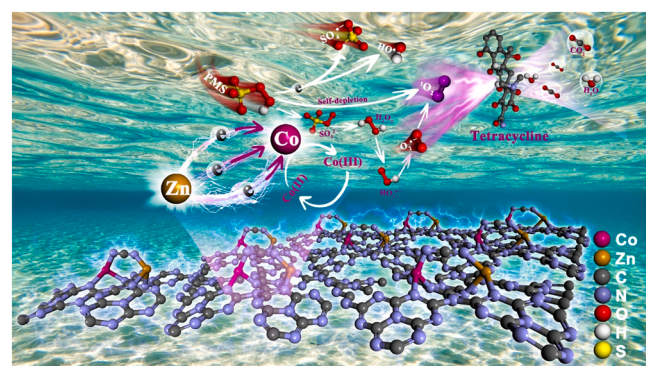
**Fig. 6.** EIS Nyquist plots of different catalysts (a); LSV curves in different reaction systems (b); Instant current over MCZC-10% after the adding of PMS and TC (c); PMS decomposition efficiencies of the synthesized catalysts (d); Geometric optimizations of PMS adsorbed onto the Co site of ZCCN and MCZC catalysts their corresponding electron density differences (e); (Yellow and lake-blue regions represent electron-rich and electron-defective areas, respectively).

in a single PMS system with poor signal intensity attributed to  $\text{TEMP}^{-1}\text{O}_2$ , which corresponded to the poor performance of TC degradation by PMS alone. The signals attributed to  $\text{TEMP}^{-1}\text{O}_2$  were captured in all three systems (Fig. 5e), with the signals in MCZC-10%/PMS exhibiting the most significant intensity, which further confirmed the non-radical pathway of TC degradation prompted by MCZC-10%/PMS.

A series of electrochemical characterizations were conducted to reveal the contribution of electron transfer to PMS activation. As shown in Fig. 6a, the EIS Nyquist plot of MCZC-10% exhibited the smallest semicircle, indicating enhanced surface charge transport properties. The linear sweep voltammetry (LSV) revealed enhanced electron transfer between MCZC-10% and PMS than direct interaction with TC (Fig. 6b) since the current density of the MCZC-10%/PMS system was higher than the MCZC-10%/TC system at a constant potential, indicating PMS was preferentially activated by MCZC-10%. This finding was further confirmed in the amperometric i-t curve (Fig. 6c), given that the instantaneous current intensity after PMS injection was significantly higher than that after TC injection. A series of systematic PMS decomposition experiments were conducted to investigate the synergistic effect between Co and Zn in activating PMS. As shown in Fig. 6d, homogeneous  $\text{Zn}^{2+}$  could hardly improve PMS decomposition performance, while PMS decomposition efficiency was improved from 37.9% to 45.2% within 24 min with homogeneous  $\text{Co}^{2+}$  and  $\text{Zn}^{2+}$ . Furthermore,  $\text{Co}_{0.5}\text{Zn}_{0.5}\text{-ZIF}$  derived MCZC-10% improved the PMS decomposition efficiency from 52.2% to 73.1% compared with ZIF-67 derived ZCCN-10% (Fig. S12). Considering the poor performance of  $\text{Zn}^{2+}$  on PMS decomposition, we hypothesize that the interaction between Co and Zn and the enhanced electron transfer to Co sites are key to the excellent performance of MCZC-10% on PMS activation.

To further investigate the exact role of Co and Zn in the activation of PMS, density functional theory calculations were carried out with detailed information shown in Text S3. As shown in Fig. 6e, the Co and Zn atoms (connected by the  $\text{N} = \text{C}-\text{N}$  bond) derived from  $\text{Co}_{0.5}\text{Zn}_{0.5}\text{-ZIF}$  or ZIF-67 were anchored in the tricyanide ring of carbon nitride with the organic skeleton structure of  $\text{Co}_{0.5}\text{Zn}_{0.5}\text{-ZIF}$  or ZIF-67 being retained. When PMS was adsorbed on the Co site of the ZCCN catalyst, the O–O bond length on PMS was extended from 1.483 Å to 1.527 Å, which made it easier for PMS to break to form  $\text{SO}_4^{2-}$  and  $\text{HO}^{\bullet}$ . In contrast, when PMS was adsorbed on the Zn site of the MCZC catalyst, the O–O bond length on PMS was slightly reduced from 1.483 Å to 1.476 Å, which made it harder to break the O–O bond and revealed the poor PMS activation performance of Zn. However, when PMS was adsorbed on the Co site on the MCZC catalyst, the O–O bond of PMS was ruptured, leading to the generation of  $\text{SO}_4^{2-}$  and  $\text{HO}^{\bullet}$ , indicating the efficient PMS activation of the MCZC catalyst. As shown in the front view of the structurally optimized ZCCN and MCZC catalysts (Fig. S13), the bond length of the Co–N bonds formed between Co atoms and  $\text{g-C}_3\text{N}_4$  on the MCZC catalyst was shortened after the replacement of adjacent Co atom to Zn atom, resulting in an enhanced electron density around the Co atom. This finding was consistent with the differential charge calculation of MCZC and ZCCN catalysts which showed that a stronger charge enrichment (with a larger area of the yellow region) at the O site was attributed to O–H on the MCZC catalyst. Moreover, unlike the apparent charge transfer between the surface of carbon nitride and the  $\text{SO}_4^{2-}$  terminal of PMS on ZCCN (with a larger area of the lake-blue region), it was not significant on MCZC, and electrons were mainly transferred to PMS through the Co sites.

Based on the above research, the radical and non-radical pathways of TC degradation by PMS activation mediated by the MCZC catalyst were proposed (Scheme 2). The PMS adsorbed on the Co site was immediately activated to form  $\text{SO}_4^{2-}$ ,  $\text{HO}^{\bullet}$ ,  $\text{O}_2^{\bullet-}$ , and  $^1\text{O}_2$  (Eq. S14–S23) with Co acting as the electron donor during the valence change from Co (II) to Co (III). With the interaction between the Co site and the adjacent Zn site, the surface electron transfer on MCZC was significantly improved since the relatively weak attraction between the outermost electron and the second outer electron increased the risk of losing the outermost two



**Scheme 2.** Proposed mechanism of MCZC/PMS system on TC degradation.

electrons under external forces of attraction. Besides, the surrounding electron-rich N groups around Co sites provided the needed electrons (extracted from Zn sites) through the C–N skeleton structure to accelerate the valence cycle from Co (III) to Co (II), which could further continue the rapid activation of PMS. And the generated  $^1\text{O}_2$  during PMS activation made the major contribution to TC degradation while  $\text{SO}_4^{2-}$ ,  $\text{O}_2^{\bullet-}$ , and  $\text{HO}^{\bullet}$  only made limited contribution, indicating that TC degradation was dominated by non-radical pathway and assisted by radical pathway.

### 3.5. Oxidation products and degradation pathways analysis

UV-vis full scan characterization (Fig. S14a) indicated a rapid degradation of TC, but the increased absorbance around 200 nm revealed the generation of intermediates, consistent with TOC measurements during the experiment with the highest mineralization rate (TOC/TOC<sub>0</sub>) reaching 55.8% within 24 min (Fig. S14b), which demonstrated comparable or greater efficiency than the reported studies in Table S5. To further identify the TC degradation process, the obtained Fukui index of TC based on DFT calculation (Text S3) helped to reveal the sites (C–C=O or C–N–C) susceptible to attacks by radicals (Fig. 7a). As electrophilic free radicals, it was easy for  $\text{SO}_4^{2-}$ ,  $\text{HO}^{\bullet}$  and  $^1\text{O}_2$  to attack the positions prone to lose electrons on TC, while the nucleophilic radical  $\text{O}_2^{\bullet-}$  was more likely to attack low-energy sites for its weak ability to extract electrons. The lowest unoccupied molecular orbital (LUMO) (Fig. 7b) and the highest occupied molecular orbital (HOMO) revealed the sites susceptible to nucleophilic reactions and electrophile reactions by escaping electrons (Fig. 7c). As expected,  $\text{O}_2^{\bullet-}$  was more likely to attack the sites located on benzene rings and oxygen-containing groups while  $\text{SO}_4^{2-}$ ,  $\text{HO}^{\bullet}$  and  $^1\text{O}_2$  were more likely to attack the sites located on nitride-containing groups. To quantify the reactivity of each atom of TC, the natural population analysis (NPA) charge distribution and Fukui index ( $f^*$ ) were calculated and listed in Fig. 7d. It was found that C2 ( $f^*=0.064$ ), C4 ( $f^*=0.0307$ ), O17 ( $f^*=0.0312$ ), O20 ( $f^*=0.0361$ ), O21 ( $f^*=0.1109$ ), O22 ( $f^*=0.0523$ ), N25 ( $f^*=0.0408$ ), O28 ( $f^*=0.0316$ ) and C29 ( $f^*=0.0297$ ) with relatively higher Fukui indexes were the more reactive sites and prone to attacks, consistent with HOMO and LUMO findings. Based on the LC-MS characterization (Table S3), the oxidation of TC initialized by  $\text{SO}_4^{2-}$  /  $\text{HO}^{\bullet}$  /  $\text{O}_2^{\bullet-}$  /  $^1\text{O}_2$  primarily occurred through radical adduct formation, hydrogen atom abstraction, and electron transfer. Three possible TC degradation pathways were further inferred (Fig. 7e). In pathway I of hydroxylation, TC was first degraded to A1 ( $m/z = 405$ ). Then the leftmost benzene ring was opened by the attack of  $\text{O}_2^{\bullet-}$  and  $-\text{NH}_2$  was removed during the carbonylation process to form A2 ( $m/z = 362$ ), which could be further degraded to A3 ( $m/z = 272$ ) and A4 ( $m/z = 226$ ) under the attack of ROS. In pathway II of deamidation, TC was first degraded to B1 ( $m/z = 325$ ) after the removal of  $-\text{NR}_2$  during the deamidation process and continued to be degraded to B2 ( $m/z = 254$ ) and B3 ( $m/z = 226$ ) under the attack of ROS. In pathway III, C1 ( $m/z = 416$ ) was formed through dehydrogenation after the loss of  $-\text{H}$ .

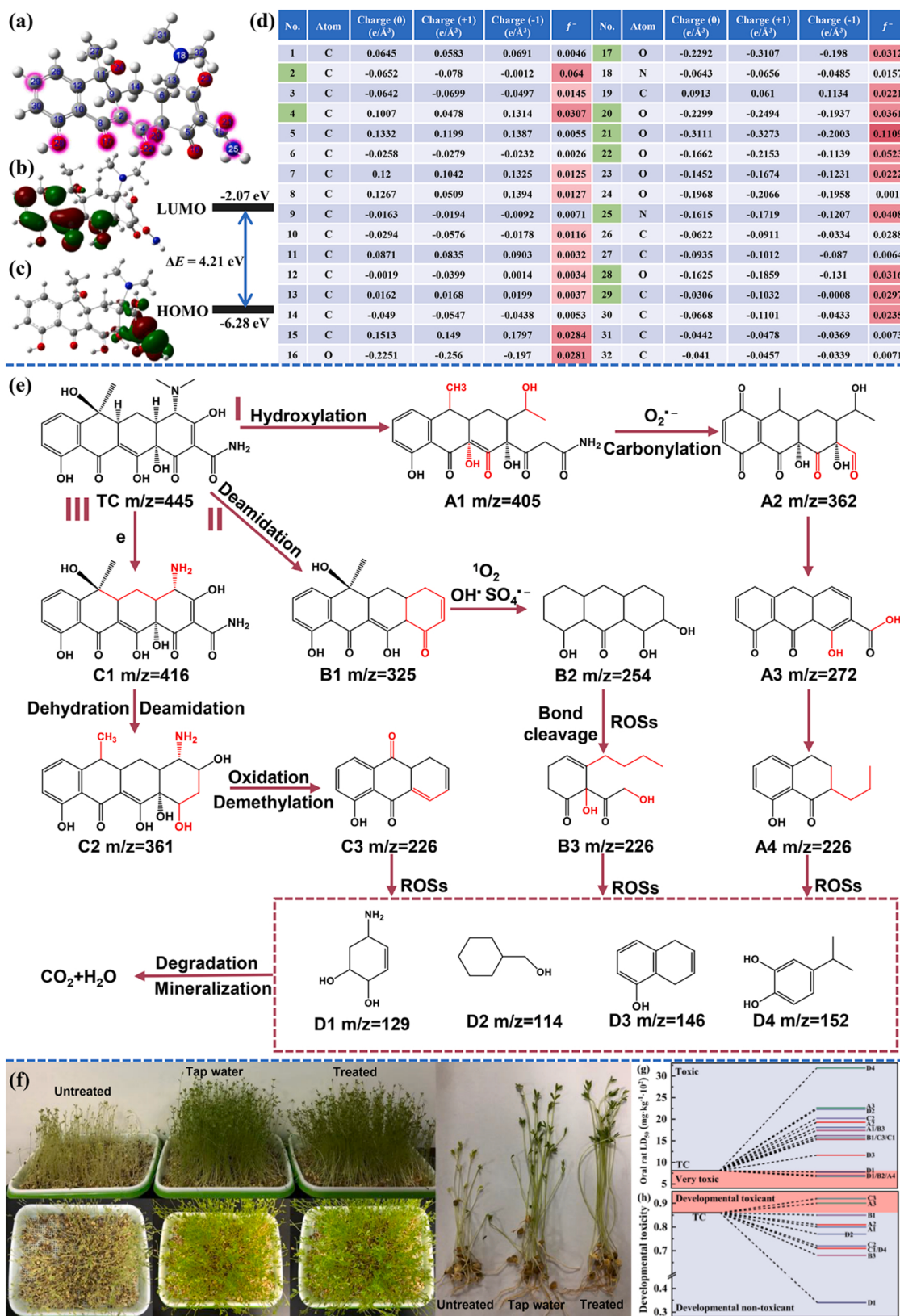


**Fig. 7.** Optimized chemical structure of TC (a); LUMO (b) and HOMO (c) of TC; NPA charge distributions and Fukui index ( $f^-$ ) of TC (d); Proposed TC degradation pathways (e); Growth of bean sprouts watered with untreated TC solution, tap water and treated TC solution (f); Acute toxicity (g) and developmental toxicity (h) of the intermediates during TC degradation.

by electrons and was further degraded to C2 ( $m/z = 361$ ) through dehydration and deamidation. Moreover, C3 ( $m/z = 226$ ) was formed through continuous oxidation and demethylation. Eventually, the formed intermediates with small molecules like D1 ( $m/z = 129$ ), D2 ( $m/z = 114$ ), D3 ( $m/z = 146$ ), and D4 ( $m/z = 152$ ) were further degraded to  $\text{CO}_2$  and  $\text{H}_2\text{O}$  by ROS.

To identify the eco-friendliness of the MCZC/PMS system in degrading TC, bean sprouts were used as a crop model with untreated TC solution, tap water, and treated TC solution used as water sources for a 20-day incubation period. As shown in Fig. 7f, the germination rate and growth of bean sprouts were significantly inhibited by untreated TC solution, while the germination rate and growth of bean sprouts watered with treated TC solution were similar to the control group watered with raw tap water, indicating the excellent performance of the MCZC/PMS system in inhibiting TC ecotoxicity. Furthermore, the acute toxicity (oral rat  $\text{LD}_{50}$ ) and developmental toxicity of the intermediates during TC degradation had been assessed by quantitative structure-activity relationship (QSAR) prediction using Toxicity Estimation Software Tool (T. E.S.T.). All intermediates except A4, B2, and D1 exhibited higher  $\text{LD}_{50}$  (Fig. 7g) with the  $RLI\% (\text{Eq. S13})$  of the treated TC solution increased from 52.3% to 92.9% (Fig. S15), which mutually corroborated the decreased acute toxicity. Besides, although no precise developmental toxicity data for D4, B2 and A4 was obtained, all the intermediates except A3 and C3 exhibiting a significant decrease in developmental toxicity (Fig. 7h), which further indicated the excellent performance of MCZC/PMS system on ecotoxicity inhibition.

### 3.6. Reusability and stability study

Considering the importance of reusability and stability of a catalyst in practical application, 21 cycles of continuous TC degradation experiments were conducted. As shown in Fig. 8a, the TC degradation efficiency decreased from 99.6% to 65.2% after 20 cycles, which might be attributed to the accumulation of intermediates on the surface of MCZC-10% that inhibited the participation of active sites in PMS activation. And the weight loss rate was calculated to be 0.3% in every cycle based on the measured initial weight of MCZC-10% (0.02 g) and final weight

of MCZC-10% (0.0188 g) after 20 cycles of TC degradation. After being thoroughly washed with deionized water, dried, and annealed at 550 °C for 2 h, the regenerated catalyst restored TC degradation efficiency to 92.4%, de-activated indicating the excellent reusability of MCZC-10%. The leaching of Co and Zn in every cycle was measured with the maximum leaching concentrations of less than 10  $\mu\text{g}\cdot\text{L}^{-1}$ , indicating that no severe secondary environmental pollution would be caused by the leaching of Co or Zn [83]. In addition, the total leached amounts of Co and Zn in 21 cycles were 9.16  $\mu\text{g}$  and 9.53  $\mu\text{g}$ , which occupied 3.46 and 3.32 wt% of the loaded Co and Zn contents in MCZC-10% (Co of 1.32 wt % and Zn of 1.38 wt%), consistent with the XPS semi-quantitative analysis of used MCZC-10% with 0.03% and 0.02% loss of Co and Zn atoms, respectively (Table S4). The utilization efficiency of MCZC-10% for TC degradation was calculated to be 0.026  $\text{mmol}\cdot\text{g}^{-1}\cdot\text{min}^{-1}$ , which exhibited higher utilization efficiency as compared to the reported catalysts of FNOC (0.001  $\text{mmol}\cdot\text{g}^{-1}\cdot\text{min}^{-1}$ ), FCOCN2 (0.0004  $\text{mmol}\cdot\text{g}^{-1}\cdot\text{min}^{-1}$ ), CuO@C-550 (0.015  $\text{mmol}\cdot\text{g}^{-1}\cdot\text{min}^{-1}$ ), PFSC-900 (0.003  $\text{mmol}\cdot\text{g}^{-1}\cdot\text{min}^{-1}$ ), B-NC (0.009  $\text{mmol}\cdot\text{g}^{-1}\cdot\text{min}^{-1}$ ), and Co@MoS<sub>2</sub> (0.005  $\text{mmol}\cdot\text{g}^{-1}\cdot\text{min}^{-1}$ ) (Fig. 8c and Table S5). XPS characterization of the catalyst before and after the experiment (Fig. 8d) exhibited the coexistence of Co (II) and Co (III), with a decrease in the content of  $\text{Co}^{2+} 2p_{2/3}$  from 59.8% to 50.8%, since the synergistic effect of Zn accelerated the transition from Co (III) to Co (II). Moreover, no apparent shifts of the diffraction peaks were observed in the XRD patterns of the fresh and used MCZC-10% catalyst, with preservation of the graphite-like structure (Fig. 8e), indicating the stable crystalline structure of MCZC-10%. And the SEM image comparison between the used catalyst and the regenerated catalyst revealed the excellent reusability of MCZC-10% for the efficient removal of accumulated intermediates and the similar hollow structure to the fresh catalyst after the regeneration (Fig. 8f). In addition, the reusability and stability of MCZC-10% were further investigated with river water as matrix and the result also revealed the good stability and reusability of MCZC-10% in practical application with the TC degradation efficiency decreased from 94.7% to 55.5% in 20 cycles but recovered to 87.6% after regeneration and the total leaching amount of Co and Zn similar to the result in deionized water (Fig. S16). In summary, the MCZC/PMS system exhibited

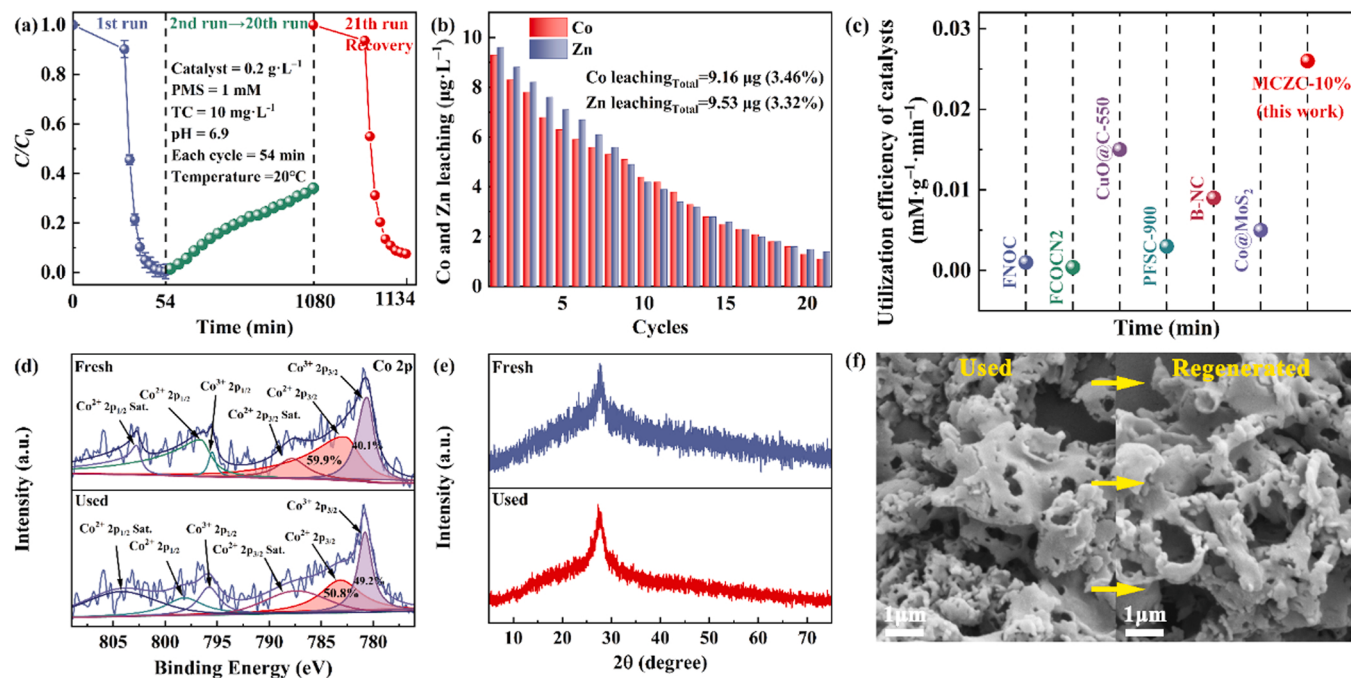


**Fig. 8.** TC degradation efficiency by MCZC-10% (a) and the corresponding Co and Zn leaching amounts (b) in 21 cycles (Catalyst dosage = 0.2 g·L<sup>-1</sup>, PMS = 1 mM, TC concentration = 10 mg·L<sup>-1</sup>, pH = 7, temperature = 20 °C); Comparison of utilization efficiencies of different catalysts (c); XPS Co 2p spectra (d), XRD patterns (e) and the SEM images (f) of the fresh and used MCZC-10%.

excellent reusability and stability in TC degradation while effectively avoiding secondary environmental pollution caused by Co/Zn leaching.

#### 4. Conclusion

In this work, a novel ZIF-derived non-bonding Co, Zn coordinated hollow carbon nitride was synthesized by etching bimetallic  $\text{Co}_{0.5}\text{Zn}_{0.5}$ -ZIF, which yielded efficient PMS activation (73.1%) and TC degradation efficiency (99.6%) over a wide pH range. Compared with the similar ZIF-67 derived catalyst ZCCN, the TC degradation efficiency was significantly improved by 32.9%, with almost half of the Co sites replaced by Zn sites. MCZC catalyst exhibited good tolerance for inorganic ions and HA and excellent PMS activation performance in the water matrix experiment. Catalytic mechanism investigation and DFT calculations revealed that the accelerated electron transfer to Co sites to enhance the valence cycle between Co (II) and Co (III) by the adjacent Zn sites was the key to the immediate breakage of the O–O bond leading to further generation of  $\text{HO}^\bullet$ ,  $\text{SO}_4^\bullet$ ,  $\text{O}_2^\bullet$ ,  $^1\text{O}_2$ . The degradation pathways of TC were proposed by LC-MS and Fukui index, with the toxicity of the intermediates accurately predicted by T.E.S.T. and the bean sprout growth, which substantiated the efficiency of the MCZC/PMS system in reducing the eco-risks caused by antibiotic contaminants. Reusability and stability experiments demonstrated that the stability of MCZC catalyst with efficient TC degradation performance was maintained, and the leaching of Co and Zn was significantly inhibited. Overall, this work developed a novel strategy to construct polymetallic MOF-derived carbon materials and provided new insights into optimizing the performance of catalysts via manipulating the interplay of adjacent inactive metal sites.

#### CRediT authorship contribution statement

**Xi Li:** Conceptualization, Methodology, Software, Writing – original draft, Writing – review & editing, Investigation, Data curation. **Shiwen Wang:** Investigation, Data curation. **Pei Chen:** Investigation, Data curation. **Baokang Xu:** Investigation, Data curation. **Xiao Zhang:** Investigation, Data curation. **Yanhua Xu:** Conceptualization, Methodology, Software, Writing – original draft, Writing – review & editing, Resources, Investigation, Funding acquisition. **Ru Zhou:** Data curation, Investigation. **Yang Yu:** Conceptualization, Methodology, Software, Writing – original draft, Writing – review & editing, Supervision, Resources, Investigation, Funding acquisition. **Huaili Zheng:** Conceptualization, Methodology, Software, Writing – original draft, Writing – review & editing, Supervision, Resources, Investigation, Funding acquisition. **Peng Yu:** Data curation, Supervision, Resources, Investigation, Methodology, Conceptualization, Funding acquisition. **Yongjun Sun:** Conceptualization, Methodology, Software, Writing – original draft, Writing – review & editing, Data curation, Resources, Supervision, Investigation, Funding acquisition.

#### Declaration of Competing Interest

The authors declare that they have no known competing financial interests or personal relationships that could have appeared to influence the work reported in this paper.

#### Data Availability

The data that has been used is confidential.

#### Acknowledgments

This work was supported by the National Natural Science Foundation of China (No. 21607074), the National Key Research and Development Program of China (2017YFB0602500), the Natural Science Foundation of Jiangsu Province in China (No. BK20201362), China Postdoctoral

Science Foundation (2022M721586), the 2018 Six Talent Peaks Project of Jiangsu Province (JNHB-038), Jiangsu Funding Program for Excellent Postdoctoral Talent (2022ZB393), and the Postgraduate Research & Practice Innovation Program of Jiangsu Province (SJCX22\_0450)). The authors also thank Shiyanjia Lab ([www.shiyanjia.com](http://www.shiyanjia.com)) for the LC-MS analysis.

#### Appendix A. Supporting information

Supplementary data associated with this article can be found in the online version at doi:[10.1016/j.apcatb.2023.122401](https://doi.org/10.1016/j.apcatb.2023.122401).

#### References

- [1] P.J. Vikesland, A. Pruden, P.J.J. Alvarez, D. Aga, H. Burgmann, X.D. Li, C. M. Manaia, I. Nambi, K. Wigginton, T. Zhang, Y.G. Zhu, Toward a comprehensive strategy to mitigate dissemination of environmental sources of antibiotic resistance, *Environ. Sci. Technol.* 51 (2017) 13061–13069.
- [2] L.X. Meng, Y.J. Sun, L. Zhu, Z.J. Lin, X.Y. Shuai, Z.C. Zhou, H. Chen, Mechanism and potential risk of antibiotic resistant bacteria carrying last resort antibiotic resistance genes under electrochemical treatment, *Sci. Total Environ.* 821 (2022) 153367.
- [3] S.A. McEwen, P.J. Collignon, Antimicrobial resistance: a one health perspective, *Microbiol. Spectr.* 6 (2018) 10, 6.2.
- [4] P. Shao, S. Yu, X. Duan, L. Yang, H. Shi, L. Ding, J. Tian, L. Yang, X. Luo, S. Wang, Potential difference driving electron transfer via defective carbon nanotubes toward selective oxidation of organic micropollutants, *Environ. Sci. Technol.* 54 (2020) 8464–8472.
- [5] P. Shao, J. Tian, F. Yang, X. Duan, S. Gao, W. Shi, X. Luo, F. Cui, S. Luo, S. Wang, Identification and regulation of active sites on nanodiamonds: establishing a highly efficient catalytic system for oxidation of organic contaminants, *Adv. Funct. Mater.* 28 (2018).
- [6] Y. Zong, X. Guan, J. Xu, Y. Feng, Y. Mao, L. Xu, H. Chu, D. Wu, Unraveling the overlooked involvement of high-valent cobalt-oxo species generated from the cobalt(II)-activated peroxymonosulfate process, *Environ. Sci. Technol.* 54 (2020) 16231–16239.
- [7] X. Zhou, C. Luo, M. Luo, Q. Wang, J. Wang, Z. Liao, Z. Chen, Z. Chen, Understanding the synergistic effect from foreign metals in bimetallic oxides for PMS activation: a common strategy to increase the stoichiometric efficiency of oxidants, *Chem. Eng. J.* 381 (2020).
- [8] Y. Xu, E. Hu, D. Xu, Q. Guo, Activation of peroxymonosulfate by bimetallic CoMn oxides loaded on coal fly ash-derived SBA-15 for efficient degradation of Rhodamine B, *Sep. Purif. Technol.* 274 (2021).
- [9] N. Liu, N. Lu, H. Yu, S. Chen, X. Quan, Degradation of aqueous bisphenol A in the CoCN/Vis/PMS system: Catalyst design, reaction kinetic and mechanism analysis, *Chem. Eng. J.* 407 (2021).
- [10] Z. Jia, J.L. Jiang, L. Sun, L.C. Zhang, Q. Wang, S.X. Liang, P. Qin, D.F. Li, J. Lu, J. J. Krušić, Role of boron in enhancing electron delocalization to improve catalytic activity of fe-based metallic glasses for persulfate-based advanced oxidation, *ACS Appl. Mater. Interfaces* 12 (2020) 44789–44797.
- [11] Z. Jia, Q. Wang, L. Sun, Q. Wang, L.C. Zhang, G. Wu, J.H. Luan, Z.B. Jiao, A. Wang, S.X. Liang, M. Gu, J. Lu, Attractive *in situ* self-reconstructed hierarchical gradient structure of metallic glass for high efficiency and remarkable stability in catalytic performance, *Adv. Funct. Mater.* 29 (2019).
- [12] S.X. Liang, Z. Jia, Y.J. Liu, W. Zhang, W. Wang, J. Lu, L.C. Zhang, Compelling rejuvenated catalytic performance in metallic glasses, *Adv. Mater.* 30 (2018), e1802764.
- [13] L.-C. Zhang, Z. Jia, F. Lyu, S.-X. Liang, J. Lu, A review of catalytic performance of metallic glasses in wastewater treatment: Recent progress and prospects, *Prog. Mater. Sci.* 105 (2019).
- [14] G.P. Anipsitakis, D.D. Dionysiou, Radical generation by the interaction of transition metals with common oxidants, *Environ. Sci. Technol.* 38 (2004) 3705–3712.
- [15] C.-C. Wang, X.-H. Yi, P. Wang, Powerful combination of MOFs and  $\text{C}_3\text{N}_4$  for enhanced photocatalytic performance, *Appl. Catal. B* 247 (2019) 24–48.
- [16] N. Rono, J.K. Kibet, B.S. Martincigh, V.O. Nyamori, A review of the current status of graphitic carbon nitride, *Crit. Rev. Solid State Mater. Sci.* 46 (2020) 189–217.
- [17] Y. Zheng, J. Liu, J. Liang, M. Jaroniec, S.Z. Qiao, Graphitic carbon nitride materials: controllable synthesis and applications in fuel cells and photocatalysis, *Energy Environ. Sci.* 5 (2012).
- [18] W.J. Ong, L.L. Tan, Y.H. Ng, S.T. Yong, S.P. Chai, Graphitic carbon nitride ( $\text{g-C}_3\text{N}_4$ )-based photocatalysts for artificial photosynthesis and environmental remediation: are we a step closer to achieving sustainability? *Chem. Rev.* 116 (2016) 7159–7329.
- [19] S. Guo, Z. Deng, M. Li, B. Jiang, C. Tian, Q. Pan, H. Fu, Phosphorus-doped carbon nitride tubes with a layered micro-nanostructure for enhanced visible-light photocatalytic hydrogen evolution, *Angew. Chem. Int. Ed. Engl.* 55 (2016) 1830–1834.
- [20] Y.-S. Jun, E.Z. Lee, X. Wang, W.H. Hong, G.D. Stucky, A. Thomas, From melamine-cyanuric acid supramolecular aggregates to carbon nitride hollow spheres, *Adv. Funct. Mater.* 23 (2013) 3661–3667.

[21] Z. Tong, D. Yang, Y. Sun, Y. Nan, Z. Jiang, Tubular g-C<sub>3</sub>N<sub>4</sub> isotype heterojunction: enhanced visible-light photocatalytic activity through cooperative manipulation of oriented electron and hole transfer, *Small* 12 (2016) 4093–4101.

[22] M. Wu, Q. Li, C. Chen, G. Su, M. Song, B. Sun, J. Meng, B. Shi, Constructed palladium-anchored hollow-rod-like graphitic carbon nitride created rapid visible-light-driven debromination of hexabromocyclododecane, *Appl. Catal. B* 297 (2021).

[23] Y. Ye, L. Gong, S. Xiang, Z. Zhang, B. Chen, Metal-organic frameworks as a versatile platform for proton conductors, *Adv. Mater.* 32 (2020) 1907090.

[24] B. Li, H.M. Wen, Y. Cui, W. Zhou, G. Qian, B. Chen, Emerging multifunctional metal-organic framework materials, *Adv. Mater.* 28 (2016) 8819–8860.

[25] W.P. Lustig, S. Mukherjee, N.D. Rudd, A.V. Desai, J. Li, S.K. Ghosh, Metal-organic frameworks: functional luminescent and photonic materials for sensing applications, *Chem. Soc. Rev.* 46 (2017) 3242–3285.

[26] L. Jiao, W. Yang, G. Wan, R. Zhang, X. Zheng, H. Zhou, S.H. Yu, H.L. Jiang, Single-atom electrocatalysts from multivariate metal-organic frameworks for highly selective reduction of CO(2) at low pressures, *Angew. Chem. Int. Ed. Engl.* 59 (2020) 20589–20595.

[27] L. Liu, X. Zhang, F. Yan, B. Geng, C. Zhu, Y. Chen, Self-supported N-doped CNT arrays for flexible Zn-air batteries, *J. Mater. Chem. A* 8 (2020) 18162–18172.

[28] S. Yang, Y. Yu, M. Dou, Z. Zhang, L. Dai, F. Wang, Two-dimensional conjugated aromatic networks as high-site-density and single-atom electrocatalysts for the oxygen reduction reaction, *Angew. Chem. Int. Ed. Engl.* 58 (2019) 14724–14730.

[29] L. Jiao, J. Zhu, Y. Zhang, W. Yang, S. Zhou, A. Li, C. Xie, X. Zheng, W. Zhou, S. H. Yu, H.L. Jiang, Non-bonding interaction of neighboring Fe and Ni single-atom pairs on MOF-derived N-doped carbon for enhanced CO(2) electroreduction, *J. Am. Chem. Soc.* 143 (2021) 19417–19424.

[30] X. Li, S. Wang, B. Xu, X. Zhang, Y. Xu, P. Yu, Y. Sun, MOF etching-induced Co-doped hollow carbon nitride catalyst for efficient removal of antibiotic contaminants by enhanced peroxymonosulfate activation, *Chem. Eng. J.* 441 (2022).

[31] R. Banerjee, A. Phan, B. Wang, C. Knobler, H. Furukawa, M. O'Keeffe, O.M. Yaghi, High-throughput synthesis of zeolitic imidazolate frameworks and application to CO<sub>2</sub> capture, *Science* 319 (2008) 939–943.

[32] A. Serrà, E. Gómez, J. Michler, L. Philippe, Facile cost-effective fabrication of Cu@Cu<sub>2</sub>O@CuO-microalgae photocatalyst with enhanced visible light degradation of tetracycline, *Chem. Eng. J.* 413 (2021), 127477.

[33] G. Lu, S. Li, Z. Guo, O.K. Farha, B.G. Hauser, X. Qi, Y. Wang, X. Wang, S. Han, X. Liu, J.S. DuChene, H. Zhang, Q. Zhang, X. Chen, J. Ma, S.C. Loo, W.D. Wei, Y. Yang, J.T. Hupp, F. Huo, Imparting functionality to a metal-organic framework material by controlled nanoparticle encapsulation, *Nat. Chem.* 4 (2012) 310–316.

[34] G. Kresse, J. Furthmuller, Efficient iterative schemes for ab initio total-energy calculations using a plane-wave basis set, *Phys. Rev. B: Condens. Matter* 54 (1996) 11169–11186.

[35] G. Kresse, J. Hafner, Ab initio molecular-dynamics simulation of the liquid-metal-amorphous-semiconductor transition in germanium, *Phys. Rev. B: Condens. Matter* 49 (1994) 14251–14269.

[36] G. Kresse, D. Joubert, From ultrasoft pseudopotentials to the projector augmented-wave method, *Phys. Rev. B* 59 (1999) 1758.

[37] P.E. Blöchl, Projector augmented-wave method, *Phys. Rev. B* 50 (1994) 17953.

[38] B. Hammer, L.B. Hansen, J.K. Nørskov, Improved adsorption energetics within density-functional theory using revised Perdew-Burke-Ernzerhof functionals, *Phys. Rev. B* 59 (1999) 7413.

[39] H.J. Monkhorst, J.D. Pack, Special points for Brillouin-zone integrations, *Phys. Rev. B* 13 (1976) 5188.

[40] X. Li, X. Zhang, S. Wang, P. Yu, Y. Xu, Y. Sun, Highly enhanced heterogeneous photo-Fenton process for tetracycline degradation by Fe/SCN Fenton-like catalyst, *J. Environ. Manag.* 312 (2022), 114856.

[41] K.S. Park, Z. Ni, A.P. Cote, J.Y. Choi, R. Huang, F.J. Uribe-Romo, H.K. Chae, M. O'Keeffe, O.M. Yaghi, Exceptional chemical and thermal stability of zeolitic imidazolate frameworks, *Proc. Natl. Acad. Sci. U. S. A.*, 103 (2006) 10186–10191.

[42] J. Sánchez-Lafínez, B. Zornoza, S. Friebé, J. Caro, S. Cao, A. Sabethgadam, B. Seoane, J. Gascon, F. Kapteijn, C. Le Guillouzer, G. Clet, M. Daturi, C. Téllez, J. Coronas, Influence of ZIF-8 particle size in the performance of polybenzimidazole mixed matrix membranes for pre-combustion CO<sub>2</sub> capture and its validation through interlaboratory test, *J. Membr. Sci.* 515 (2016) 45–53.

[43] J. Tang, R.R. Salunkhe, H. Zhang, V. Malgras, T. Ahamad, S.M. Alshehri, N. Kobayashi, S. Tominaka, Y. Ide, J.H. Kim, Y. Yamauchi, Bimetallic metal-organic frameworks for controlled catalytic graphitization of nanoporous carbons, *Sci. Rep.* 6 (2016) 30295.

[44] N.L. Torad, M. Hu, Y. Kamachi, K. Takai, M. Imura, M. Naito, Y. Yamauchi, Facile synthesis of nanoporous carbons with controlled particle sizes by direct carbonization of monodispersed ZIF-8 crystals, *Chem. Commun.* 49 (2013) 2521–2523.

[45] N.L. Torad, M. Hu, S. Ishihara, H. Sukegawa, A.A. Belik, M. Imura, K. Ariga, Y. Sakka, Y. Yamauchi, Direct synthesis of MOF-derived nanoporous carbon with magnetic Co nanoparticles toward efficient water treatment, *Small* 10 (2014) 2096–2107.

[46] Z.X. Cai, Z.L. Wang, Y.J. Xia, H. Lim, W. Zhou, A. Taniguchi, M. Ohtani, K. Kobiro, T. Fujita, Y. Yamauchi, Tailored catalytic nanoframes from metal-organic frameworks by anisotropic surface modification and etching for the hydrogen evolution reaction, *Angew. Chem. Int. Ed. Engl.* 60 (2021) 4747–4755.

[47] F. Asadi, S.N. Azizi, S. Ghasemi, Preparation of Ag nanoparticles on nano cobalt-based metal organic framework (ZIF-67) as catalyst support for electrochemical determination of hydrazine, *J. Mater. Sci.: Mater. Electron.* 30 (2019) 5410–5420.

[48] H. Li, C. Shan, B. Pan, Fe (III)-doped g-C<sub>3</sub>N<sub>4</sub> mediated peroxymonosulfate activation for selective degradation of phenolic compounds via high-valent iron-oxo species, *Environ. Sci. Technol.* 52 (2018) 2197–2205.

[49] Q. Li, J. Yang, D. Feng, Z. Wu, Q. Wu, S.S. Park, C.-S. Ha, D. Zhao, Facile synthesis of porous carbon nitride spheres with hierarchical three-dimensional mesostructures for CO<sub>2</sub> capture, *Nano Res.* 3 (2010) 632–642.

[50] W. Peng, S. Liu, H. Sun, Y. Yao, L. Zhi, S. Wang, Synthesis of porous reduced graphene oxide as metal-free carbon for adsorption and catalytic oxidation of organics in water, *J. Mater. Chem. A* 1 (2013).

[51] X. Zhang, B. Xu, S. Wang, X. Li, B. Liu, Y. Xu, P. Yu, Y. Sun, High-density dispersion of CuN(x) sites for H(2)O(2) activation toward enhanced Photo-Fenton performance in antibiotic contaminant degradation, *J. Hazard. Mater.* 423 (2022), 127039.

[52] G. Chen, S. He, G. Shi, Y. Ma, C. Ruan, X. Jin, Q. Chen, X. Liu, H. Dai, X. Chen, D. Huang, In-situ immobilization of ZIF-67 on wood aerogel for effective removal of tetracycline from water, *Chem. Eng. J.* 423 (2021).

[53] L. Zou, C.C. Hou, Z. Liu, H. Pang, Q. Xu, Superlong single-crystal metal-organic framework nanotubes, *J. Am. Chem. Soc.* 140 (2018) 15393–15401.

[54] Y. Yao, H. Yin, Y. Zhang, F. Wei, H. Hu, Y. Tang, S. Wang, Fe, Cu-coordinated ZIF-derived bimetal encapsulated N-doped carbon nanotube for efficient remediation of various aqueous pollutants, *Chem. Eng. J.* 426 (2021).

[55] Y. Hou, M. Qiu, T. Zhang, J. Ma, S. Liu, X. Zhuang, C. Yuan, X. Feng, Efficient electrochemical and photoelectrochemical water splitting by a 3D nanostructured carbon supported on flexible exfoliated graphene foil, *Adv. Mater.* 29 (2017).

[56] W. Zang, A. Sumbjo, Y. Ma, H. Zhang, Y. Wu, S. Wu, H. Wu, Z. Liu, C. Guan, J. Wang, S.J. Pennycook, Single Co atoms anchored in porous N-doped carbon for efficient zinc–air battery cathodes, *ACS Catal.* 8 (2018) 8961–8969.

[57] X. Li, W. Zhang, Z. Liu, S. Wang, X. Zhang, B. Xu, P. Yu, Y. Xu, Y. Sun, Effective removal of tetracycline from water by catalytic peroxymonosulfate oxidation over Co@MoS<sub>2</sub>; catalytic performance and degradation mechanism, *Sep. Purif. Technol.* 294 (2022).

[58] X. Li, S. Wang, X. Zhang, D. Mei, Y. Xu, P. Yu, Y. Sun, Nonthermal plasma catalysis enhances simultaneous removal of toluene and ozone over TiO<sub>2</sub>@ZIF-8, *J. Clean. Prod.* 332 (2022).

[59] Y. Hong, J. Peng, X. Zhao, Y. Yan, B. Lai, G. Yao, Efficient degradation of atrazine by CoMgAl layered double oxides catalyzed peroxymonosulfate: optimization, degradation pathways and mechanism, *Chem. Eng. J.* 370 (2019) 354–363.

[60] Z. Wu, Z. Tong, Y. Xie, H. Sun, X. Gong, P. Qin, Y. Liang, X. Yuan, D. Zou, L. Jiang, Efficient degradation of tetracycline by persulfate activation with Fe, Co and O co-doped g-C<sub>3</sub>N<sub>4</sub>: Performance, mechanism and toxicity, *Chem. Eng. J.* 434 (2022).

[61] Y. Fan, Y. Liu, X. Hu, Z. Sun, Preparation of metal organic framework derived materials CoFe<sub>2</sub>O<sub>4</sub>@NC and its application for degradation of norfloxacin from aqueous solutions by activated peroxymonosulfate, *Chemosphere* 275 (2021), 130059.

[62] X. Xu, G. Pliego, J.A. Zazo, J.A. Casas, J.J. Rodriguez, Mineralization of naphthenic acids with thermally-activated persulfate: the important role of oxygen, *J. Hazard. Mater.* 318 (2016) 355–362.

[63] J. Zhu, J. Wang, C. Shan, J. Zhang, L. Lv, B. Pan, Durable activation of peroxymonosulfate mediated by Co-doped mesoporous FePO<sub>4</sub> via charge redistribution for atrazine degradation, *Chem. Eng. J.* 375 (2019).

[64] X. Long, S. Yang, X. Qiu, D. Ding, C. Feng, R. Chen, Jihua Tan, X. Wang, N. Chen, Q. Lei, Heterogeneous activation of peroxymonosulfate for bisphenol A degradation using CoFe<sub>2</sub>O<sub>4</sub> derived by hybrid cobalt-ion hexacyanoferrate nanoparticles, *Chem. Eng. J.* 404 (2021).

[65] P. Hu, M. Long, Cobalt-catalyzed sulfate radical-based advanced oxidation: a review on heterogeneous catalysts and applications, *Appl. Catal. B* 181 (2016) 103–117.

[66] J. Deng, S. Feng, K. Zhang, J. Li, H. Wang, T. Zhang, X. Ma, Heterogeneous activation of peroxymonosulfate using ordered mesoporous Co<sub>3</sub>O<sub>4</sub> for the degradation of chloramphenicol at neutral pH, *Chem. Eng. J.* 308 (2017) 505–515.

[67] G. Lv, T. Wang, X. Zou, J. Shen, J. Wang, Y. Chen, F. Wang, X. Zhang, Highly dispersed copper oxide-loaded hollow Fe-MFI zeolite for enhanced tetracycline degradation, *Colloids Surf. A* 655 (2022).

[68] X. Lai, X.A. Ning, J. Chen, Y. Li, Y. Zhang, Y. Yuan, Comparison of the Fe(2+)/H(2)O(2) and Fe(2+)/PMS systems in simulated sludge: removal of PAHs, migration of elements and formation of chlorination by-products, *J. Hazard. Mater.* 398 (2020), 122826.

[69] J. Lee, U. von Gunten, J.H. Kim, Persulfate-based advanced oxidation: critical assessment of opportunities and roadblocks, *Environ. Sci. Technol.* 54 (2020) 3064–3081.

[70] X. Zhou, C. Luo, M. Luo, Q. Wang, J. Wang, Z. Liao, Z. Chen, Z. Chen, Understanding the synergistic effect from foreign metals in bimetallic oxides for PMS activation: A common strategy to increase the stoichiometric efficiency of oxidants, *Chem. Eng. J.* 381 (2020), 122587.

[71] X. Zhao, Q.-D. An, Z.-Y. Xiao, S.-R. Zhai, Z. Shi, Seaweed-derived multifunctional nitrogen/cobalt-codoped carbonaceous beads for relatively high-efficient peroxymonosulfate activation for organic pollutants degradation, *Chem. Eng. J.* 353 (2018) 746–759.

[72] Y.H. Huang, Y.F. Huang, C.I. Huang, C.Y. Chen, Efficient decolorization of azo dye Reactive Black B involving aromatic fragment degradation in buffered Co<sup>2+</sup>/PMS oxidative processes with a ppb level dosage of Co<sup>2+</sup>-catalyst, *J. Hazard. Mater.* 170 (2009) 1110–1118.

[73] L. Tang, C. Feng, Y. Deng, G. Zeng, J. Wang, Y. Liu, H. Feng, J. Wang, Enhanced photocatalytic activity of ternary Ag/g-C<sub>3</sub>N<sub>4</sub>/NaTaO<sub>3</sub> photocatalysts under wide

spectrum light radiation: the high potential band protection mechanism, *Appl. Catal. B* 230 (2018) 102–114.

[74] H. Shi, Y. He, Y. Li, T. He, P. Luo, Efficient degradation of tetracycline in real water systems by metal-free g-C<sub>3</sub>N<sub>4</sub> microsphere through visible-light catalysis and PMS activation synergy, *Sep. Purif. Technol.* 280 (2022).

[75] L. Niu, G. Zhang, G. Xian, Z. Ren, T. Wei, Q. Li, Y. Zhang, Z. Zou, Tetracycline degradation by persulfate activated with magnetic  $\gamma$ -Fe<sub>2</sub>O<sub>3</sub>/CeO<sub>2</sub> catalyst: performance, activation mechanism and degradation pathway, *Sep. Purif. Technol.* 259 (2021).

[76] X. Peng, J. Wu, Z. Zhao, X. Wang, H. Dai, Y. Wei, G. Xu, F. Hu, Activation of peroxymonosulfate by single atom Co-N-C catalysts for high-efficient removal of chloroquine phosphate via non-radical pathways: electron-transfer mechanism, *Chem. Eng. J.* 429 (2022).

[77] K.Z. Huang, H. Zhang, Direct electron-transfer-based peroxymonosulfate activation by iron-doped manganese oxide ( $\delta$ -MnO<sub>2</sub>) and the development of galvanic oxidation processes (GOPs), *Environ. Sci. Technol.* 53 (2019) 12610–12620.

[78] B. Sun, W. Ma, N. Wang, P. Xu, L. Zhang, B. Wang, H. Zhao, K.A. Lin, Y. Du, Polyaniline: a new metal-free catalyst for peroxymonosulfate activation with highly efficient and durable removal of organic pollutants, *Environ. Sci. Technol.* 53 (2019) 9771–9780.

[79] X. Zhang, B. Ren, X. Li, Y. Xu, B. Liu, P. Yu, Y. Sun, D. Mei, Efficiently enhanced visible-light photocatalytic activity by in situ deposition of Ag@AgBr on g-C<sub>3</sub>N<sub>4</sub>/Fe<sub>3</sub>O<sub>4</sub> magnetic heterogeneous materials, *Sep. Purif. Technol.* 254 (2021).

[80] W. Ren, L. Xiong, X. Yuan, Z. Yu, H. Zhang, X. Duan, S. Wang, Activation of peroxydisulfate on carbon nanotubes: electron-transfer mechanism, *Environ. Sci. Technol.* 53 (2019) 14595–14603.

[81] Z. Huang, Y. Yao, J. Lu, C. Chen, W. Lu, S. Huang, W. Chen, The consortium of heterogeneous cobalt phthalocyanine catalyst and bicarbonate ion as a novel platform for contaminants elimination based on peroxymonosulfate activation, *J. Hazard. Mater.* 301 (2016) 214–221.

[82] J. Wang, S. Wang, Reactive species in advanced oxidation processes: Formation, identification and reaction mechanism, *Chem. Eng. J.* 401 (2020), 126158.

[83] G.P. Anipsitakis, E. Stathatos, D.D. Dionysiou, Heterogeneous activation of oxone using Co<sub>3</sub>O<sub>4</sub>, *J. Phys. Chem. B* 109 (2005) 13052–13055.